

2007

## Plasma spectroscopy methods for diagnostics in the synthesis of nanostructured materials

Adam Richard Waite  
*University of Dayton*

Follow this and additional works at: [https://ecommons.udayton.edu/graduate\\_theses](https://ecommons.udayton.edu/graduate_theses)

---

### Recommended Citation

Waite, Adam Richard, "Plasma spectroscopy methods for diagnostics in the synthesis of nanostructured materials" (2007). *Graduate Theses and Dissertations*. 6189.  
[https://ecommons.udayton.edu/graduate\\_theses/6189](https://ecommons.udayton.edu/graduate_theses/6189)

This Thesis is brought to you for free and open access by the Theses and Dissertations at eCommons. It has been accepted for inclusion in Graduate Theses and Dissertations by an authorized administrator of eCommons. For more information, please contact [mschlangen1@udayton.edu](mailto:mschlangen1@udayton.edu), [ecommons@udayton.edu](mailto:ecommons@udayton.edu).

**PLASMA SPECTROSCOPY METHODS FOR DIAGNOSTICS IN THE  
SYNTHESIS OF NANOSTRUCTURED MATERIALS**

Thesis  
Submitted to  
The School of Engineering of the  
UNIVERSITY OF DAYTON

In Partial Fulfillment of the Requirements for

The Degree

Master of Science in Materials Engineering

By

Adam Richard Waite

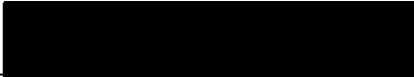
UNIVERSITY OF DAYTON


Dayton, Ohio

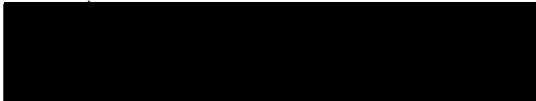
April 2007

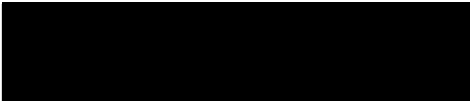
PLASMA SPECTROSCOPY METHODS FOR DIAGNOSTICS IN THE SYNTHESIS  
OF NANOSTRUCTURED MATERIALS

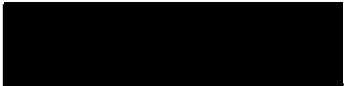
APPROVED BY:

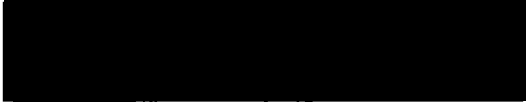
  
Andrey A. Voevodin, Ph.D.  
Advisory Committee Chairman  
Professor  
Materials Engineering Department

  
Christopher Muratore, Ph.D.  
Advisory Committee Member  
Visiting Scientist  
Air Force Research Laboratory

  
John G. Jones, Ph.D.  
Advisory Committee Member  
Senior Materials Research Engineer  
Air Force Research Laboratory

  
Paul T. Murray, Ph.D.  
Advisory Committee Member  
Professor  
Materials Engineering Department

  
Donald L. Moon, Ph.D.  
Associate Dean  
Graduate Engineering Programs & Research  
School of Engineering

  
Joseph E. Saliba, Ph.D., P.E.  
Dean, School of Engineering

To Mom and Dad

## **ABSTRACT**

### **PLASMA SPECTROSCOPY METHODS FOR DIAGNOSTICS IN THE SYNTHESIS OF NANOSTRUCTURED MATERIALS**

Name: Waite, Adam Richard

University of Dayton, 2007

Advisory Committee Chairman: Dr. Andrey A. Voevodin

Three nanostructured materials in which a plasma process was utilized to deposit a coating or modify a material were studied with in situ optical plasma diagnostics. Carbon nanotube plasma functionalization, IBPLD of aluminum oxynitride, and MSPLD of yttria stabilized zirconia and molybdenum were studied in order to correlate real-time in situ plasma data with ex situ coating analyses in order to facilitate increased process control. This increased process control is required in order to scale up these coating processes from laboratory deposition scale to full industrial fabrication. In the functionalization of carbon nanotubes with nitrogen/argon and hydrogen/argon plasmas, the reactive gas content and species in the plasma was correlated to the degree of functionalization and surface damage. It was shown that higher concentrations of the reactive gas in the plasma increased surface damage as well as increased the degree of functionalization. In the aluminum oxynitride IBPLD process, the coupling of the two plasma sources produced NO species in the plasma which was correlated to film

properties. This NO species was not present in either plasma source while operating alone and suggests this species is a key part of the growth mechanism for aluminum oxynitride. The yttria stabilized zirconia and molybdenum nanocomposite was formed with amorphous molybdenum and nanocrystalline zirconia. Normally, zirconia forms crystals at very high temperatures and pressures, but that would cause crystal growth in molybdenum as well. This apparent paradox in coating properties was explained with time resolved ICCD imaging. The imaging showed a secondary emission from the slower moving neutral species in the laser ablation plume. This excitation was hypothesized to be the result of a large increase in current as the magnetron recovered from a perceived arc event.

## **ACKNOWLEDGEMENTS**

Special thanks are required to Dr. Andrey Voevodin, Dr. John Jones, Dr. Chris Muratore, and Dr. Terry Murray. Without their support, patience, and time (especially proofreading and editing), this thesis and my Masters degree would not have been completed in the timely manner it has. I am thankful for all that you have done for me.

The author would like to acknowledge:

All of my co-workers (which I would surely forget someone if I were to try to list everyone) for making my time in MLBT for my Masters degree the best job I've ever had;

Ben "Five Year Thesis" Phillips of the Air Force Research Labs for general advice in the thesis process and formatting;

Dr. John Grant of UDRI for XPS/AES instruction;

Zach West of UDRI and AFRL/PRTG for many lengthy discussions about plasma interactions over beverages and darts;

Above all, my family, who have always been there for me, and have always believed in me.

Work presented in this thesis can also be found in the following journal articles:

Jones, J. G., Muratore, C., Waite, A. R., and Voevodin, A. A., 2006, "Plasma diagnostics of hybrid magnetron sputtering and pulsed laser deposition", *Surface and Coatings Technology* 201: 4040-4045.

Jones, J. G., Muratore, C., Waite, A. R., and Voevodin, A. A., 2007, "Plasma Treatment of Carbon Nanotubes", *Journal of Vacuum Science & Technology B*, (In Press).

Voevodin, A. A., Jones, J. G., Zabinski, J. S., and Waite, A. R., 2007, "Plasma Interaction Effects in Ion-Beam Assisted Pulsed Laser Deposition of Al-O-N Films", *Journal of Applied Physics*, (In Press).



## TABLE OF CONTENTS

<b>ABSTRACT.....</b>	<b>iv</b>
<b>ACKNOWLEDGEMENTS.....</b>	<b>vi</b>
<b>LIST OF FIGURES .....</b>	<b>x</b>
<b>LIST OF TABLES .....</b>	<b>xii</b>
 <b>CHAPTER 1: INTRODUCTION AND BACKGROUND.....</b>	 <b>1</b>
<b>1.1 Thesis Introduction .....</b>	<b>1</b>
<b>1.2 Ex Situ Coating Analysis Tools.....</b>	<b>7</b>
<b>1.2.1 X-Ray Photoelectron Spectroscopy .....</b>	<b>7</b>
<b>1.2.2 X-Ray Diffraction.....</b>	<b>9</b>
<b>1.2.3 Raman Spectroscopy.....</b>	<b>10</b>
<b>1.2.4 Electron Microscopies.....</b>	<b>10</b>
<b>1.2.5 Ball-on-Flat Tribometer .....</b>	<b>11</b>
<b>1.3 Electrostatic In Situ Plasma Analysis Tools .....</b>	<b>11</b>
<b>1.3.1 Langmuir Probe .....</b>	<b>11</b>
<b>1.3.2 Electrostatic Quadrupole Plasma (EQP) Analyzer.....</b>	<b>13</b>
<b>1.4 Optical In Situ Plasma Analysis Tools .....</b>	<b>15</b>
<b>1.4.1 Intensified Charge-Coupled Device (ICCD) Plasma Imaging .....</b>	<b>15</b>
<b>1.4.2 Optical Emission Spectroscopy .....</b>	<b>15</b>
<b>1.4.3 Time of Flight Analysis.....</b>	<b>16</b>
<b>1.5 Introduction to Individual Experiments .....</b>	<b>17</b>
<b>1.5.1 Introduction to Plasma Functionalization of Carbon Nanotubes .....</b>	<b>17</b>
<b>1.5.2 Introduction to IBPLD of Aluminum Oxynitride.....</b>	<b>19</b>
<b>1.5.3 Introduction to MSPLD of Yttria Stabilized Zirconia and Molybdenum .....</b>	<b>20</b>
 <b>CHAPTER 2: EXPERIMENTAL PROCEDURES.....</b>	 <b>22</b>

<b>2.1 Experimental Procedures for Plasma Functionalization of Carbon Nanotubes</b>	22
2.1.1 Carbon Nanotube Sample Treatment	22
2.1.2 Plasma Data Collection	24
2.1.3 Functionalized Carbon Nanotube Data Collection	24
<b>2.2 Experimental Procedures for IBPLD of Aluminum Oxynitride</b>	26
2.2.1 Sample Preparation and Coating Deposition	26
2.2.2 Plasma Data Collection	28
2.2.3 Coating Data Collection	29
<b>2.3 Experimental Procedures for MSPLD of Yttria Stabilized Zirconia and Molybdenum Nanocomposite</b>	29
2.3.1 Sample Preparation and Coating Deposition	29
2.3.2 Plasma Data Collection	32
2.3.3 Coating Data Collection	33
<b>CHAPTER 3: RESULTS AND DISCUSSION</b>	34
<b>3.1 Analysis and Discussion of Plasma Functionalization of Carbon Nanotubes</b>	34
3.1.1 Plasma Diagnostics Analysis	34
3.1.2 Coatings Analysis	37
3.1.3 Discussion	44
<b>3.2 Analysis and Discussion of IBPLD of Aluminum Oxynitride</b>	50
3.2.1 Plasma Diagnostics Analysis	50
3.2.2 Coatings Analysis	53
3.2.3 Discussion	61
<b>3.3 Analysis and Discussion of MSPLD of Yttria Stabilized Zirconia and Molybdenum Nanocomposite</b>	63
3.3.1 Plasma Diagnostics Analysis	63
3.3.2 Coatings Analysis	69
3.3.3 Discussion	73
<b>CHAPTER 4: CONCLUSIONS</b>	75

## LIST OF FIGURES

Figure 1: Process Control Schematic with In Situ Plasma Diagnostics and Ex Situ Materials Analyses.....	2
Figure 2: Pin-on-Disk Tribometer Schematic.....	5
Figure 3: Section of a plasma discharge tube that a probe can be inserted with an undisturbed plasma (a) and a probe disturbed plasma (b) .....	6
Figure 4: Thesis Overview.....	8
Figure 5: Sample Langmuir Chart .....	12
Figure 6: Schematic of an electrostatic quadrupole plasma analyzer .....	14
Figure 7: Carbon nanotube functionalization chamber schematic.....	25
Figure 8: Aluminum oxynitride deposition chamber schematic.....	27
Figure 9: Yttria stabilized zirconia and molybdenum deposition schematic .....	30
Figure 10: OES for all H <sub>2</sub> /Ar plasma gas mixtures.....	35
Figure 11: OES for all N <sub>2</sub> /Ar plasma gas mixtures.....	36
Figure 12: As received XPS scans of carbon nanotube samples .....	39
Figure 13: XPS scans of carbon nanotube samples after 5 second plasma cleaning .....	40
Figure 14: XPS scans of carbon nanotube samples after 45 second plasma treatment ....	41
Figure 15: High resolution XPS scans of carbon nanotube C 1s peak - as received sample (a), sample after 45 second 20% H <sub>2</sub> /80% Ar plasma treatment (b), and sample after 45 second 20% N <sub>2</sub> /80% Ar plasma treatment (c) .....	43

Figure 16: Carbon nanotube SEM micrographs of as received sample (a), 80% N <sub>2</sub> /20% Ar plasma (b), 20% N <sub>2</sub> /80% Ar plasma (c), 80% H <sub>2</sub> /20% Ar plasma (d), and 20% H <sub>2</sub> /80% Ar plasma (e) .....	45
Figure 17: Temperature vs. chamber pressure in the outgassing of a carbon nanotube sample on Inconel .....	48
Figure 18: OES spectra from IBPLD process - PLD of Al (a), Ion beam with N <sub>2</sub> gas (b), and combined PLD of Al and ion beam in N <sub>2</sub> gas (c).....	51
Figure 19: ICCD imaging of PLD of Al <sub>2</sub> O <sub>3</sub> target (a) and IBPLD process (b) with varying N <sub>2</sub> background pressure .....	54
Figure 20: IBPLD of Al <sub>2</sub> O <sub>3</sub> target in N <sub>2</sub> background at 20 mTorr with spectral filters ...	55
Figure 21: Background N <sub>2</sub> gas pressure versus atomic composition of sample as determined by XPS .....	56
Figure 22: Background N <sub>2</sub> gas pressure versus N%/Al% ratio in sample as determined by XPS .....	58
Figure 23: Ion beam energy versus atomic composition of sample as determined by XPS .....	59
Figure 24: XRD of Al-O-N samples with and without substrate bias .....	60
Figure 25: Voltage and current waveforms versus time for the magnetron in the MSPLD process with 1) initiation and sputtering, 2) shutoff and recovery, and 3) voltage transition for reinitiation operational modes .....	64
Figure 26: TOF waveforms of PLD of YSZ target .....	66
Figure 27: ICCD imaging of MSPLD process with a typical laser plume response .....	67
Figure 28: ICCD imaging of MSPLD process with a secondary laser plume interaction and emission response.....	68
Figure 29: Voltage waveform and ZrO* TOF at 6 μs synchronization delay for laser trigger from magnetron .....	70
Figure 30: XRD scans of YSZ/Mo nanocomposite coatings with no synchronization, 1 μs synchronization, 4 μs synchronization, and 6 μs synchronization .....	72

## LIST OF TABLES

Table 1: Carbon nanotube functionalization plasma parameters .....	23
Table 2: All identified OES plasma species in carbon nanotube functionalization plasmas .....	38
Table 3: All identified OES plasma species in IBPLD plasma processes .....	52
Table 4: Atomic composition of MSPLD coatings with no synchronization, 1 $\mu$ s delay synchronization, and 6 $\mu$ s delay synchronization as determined by XPS.....	71

## **CHAPTER 1**

### **INTRODUCTION AND BACKGROUND**

#### **1.1 Thesis Introduction**

The next evolutionary step in materials science is in nanostructured materials. As technology improves, manipulation of smaller and smaller amounts of matter will allow further control of material properties. While most of the research is taking place in the development of these nanostructured materials, research must also begin for the transition from research synthesis to industrial manufacture. This especially applies to plasma based processes of coating synthesis, where resulting nanostructures strongly depend on plasma process characteristics. One facet of the nanostructured coating technology will be materials characterization and analysis, ex situ and in situ. In an industrial scale up, relying solely on ex situ analysis of a coating is unacceptable. Knowing what is going on in the process, during that process, is the key to producing a high quality, reproducible product. Without this in situ process input, process control becomes difficult at best.

Figure 1 is a schematic of how in situ analysis is important for industrial scale up. First, a plasma process must be chosen in order to synthesized and/or process a nanostructured material such as a nanocomposite, functionalized carbon nanotube, or nanostructured ceramic. In situ diagnostics must be performed in order to determine plasma characteristics such as plasma chemistry, energy, density, and excitation states.

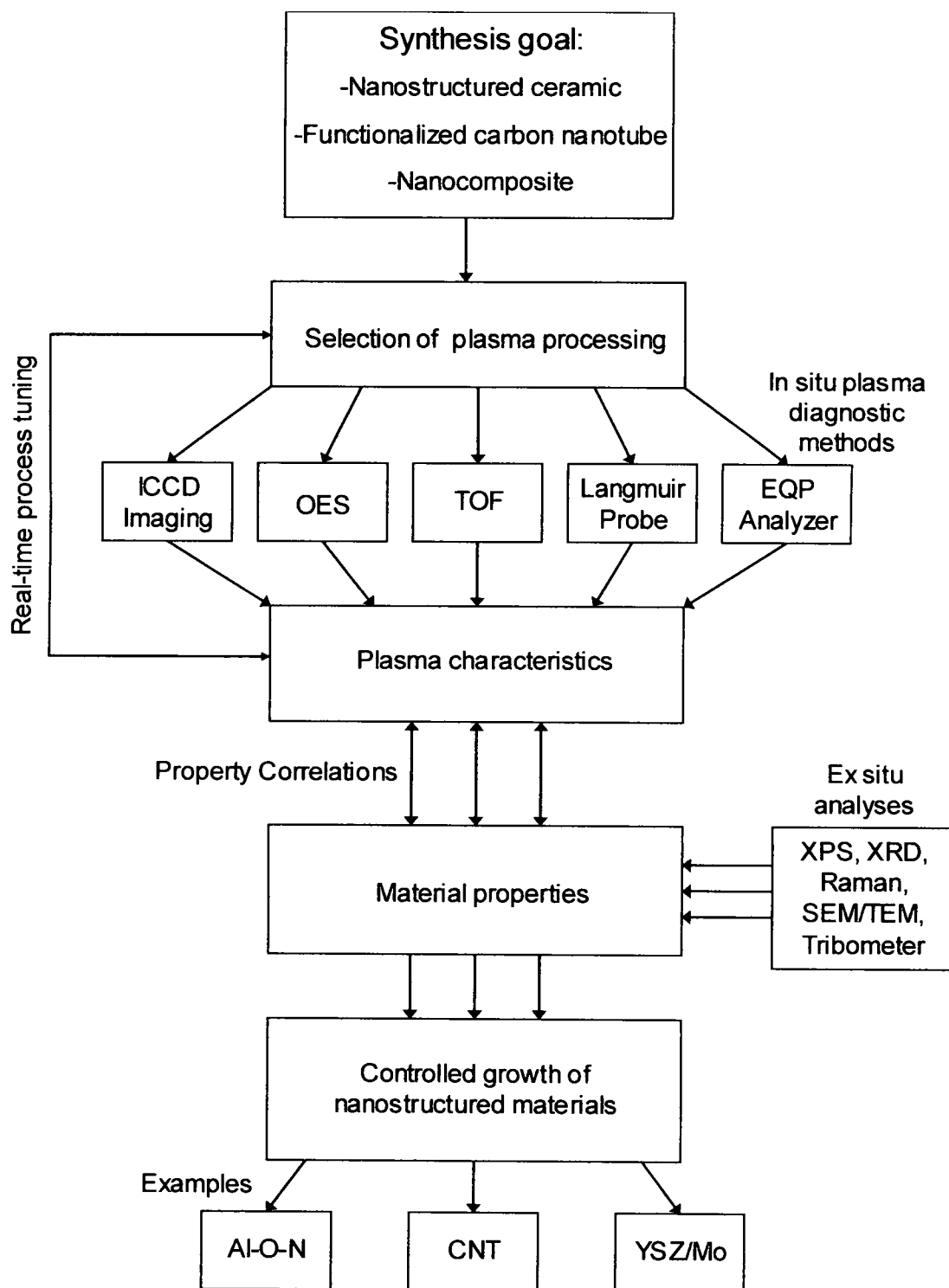


Figure 1: Process Control Schematic with In Situ Plasma Diagnostics and Ex Situ Materials Analyses

After the plasma processing, ex situ analysis is performed in order to study material properties such as chemistry, structural, mechanical, and tribological properties. After correlating material properties to plasma properties, real-time process control tuning can be performed. The final result of this work is the controlled growth of nanostructured materials, of which three examples which are outline in this thesis. These examples are aluminum oxynitride (a nanostructured ceramic), functionalized carbon nanotubes, and a yttria stabilized zirconia and molybdenum nanocomposite.

The main focus of this research is the development of nanostructured materials for tribological applications. Each application is intended to be part of a solid lubricant system that would have give an optimum mix of toughness, a low friction coefficient, and low wear rates in multiple environments. Tribological “chameleon” coatings are coatings that can change their surface chemistry and microstructure to adapt to environmental or loading changes [1]. These “chameleon” coatings have the ability to reversibly change in response to humidity, temperature, and load changes. This class of nanostructured coatings would allow for excellent friction and wear performance cycling between extreme environments such as ambient atmosphere, to space, and back to ambient atmosphere.

In the realm of nanostructured coatings, there are three main groups of coating characterization tools: 1) ex situ coatings analysis, 2) in situ electrostatic plasma analysis, and 3) in situ optical plasma analysis. Ex situ coating analyses are performed after the coating has been deposited on the substrate. The main advantage is that the chemistry, structure, and any performance characteristics can be tested directly. The primary disadvantage is that all these analyses are performed after the deposition is complete.



Without an in-process analysis, reproducibility and coating quality will suffer. This is due to current deposition technology being batch processes, where it is too late to correct any problems if characterization is performed ex situ. In situ diagnostics allow for correction during production. Examples of a few ex situ characterization methods include X-ray photoelectron spectroscopy (XPS), X-ray diffraction (XRD), Raman spectroscopy, electron microcopies (SEM and TEM), and for tribological coatings, ball-on-flat tribometer analysis (Figure 2).

In situ electrostatic plasma analysis is a set of in process analysis tools that are inserted directly into a plasma during the deposition process. This offers the advantage of real-time time process feedback, at an exact point of interest in the plasma. The major drawback is that by having a charged probe in the actual plasma, the probe itself disturbs the plasma. An example of a charged probe inserted in a plasma can be seen in Figure 3 [2]. Not only is there a disturbance around the probe, but there are further disturbances in the plasma in the direction of the anode on the right. Two example analysis tools are a Langmuir probe and an electrostatic quadrupole plasma (EQP) analyzer.

In situ optical plasma analysis comprises a set of analyses that relies on the spectral emissions radiated from the plasma process. The advantage of this set of techniques is that it can give real-time feedback without an effect on the actual plasma and coating deposition process. The drawback is that the data is an average over a certain area for a set period of time, not a specific value at a certain point. This drawback is the result from taking information about a three dimensional process and converting it into a two dimensional output. A few examples of optical plasma analysis tools are intensified

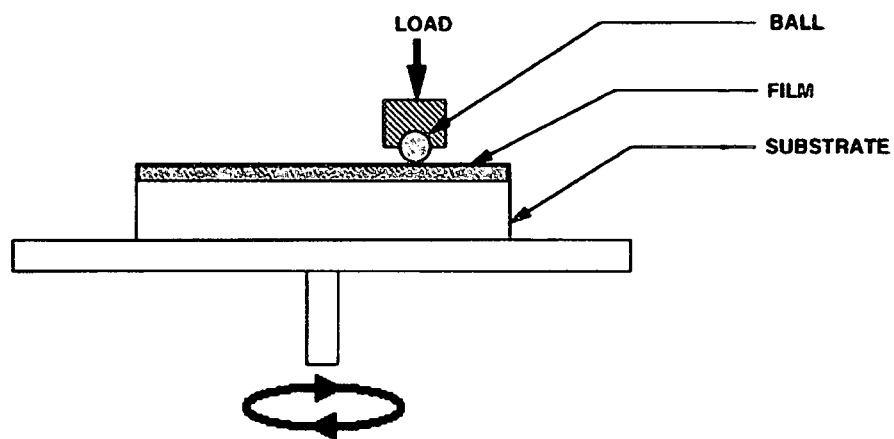


Figure 2: Pin-on-Disk Tribometer Schematic

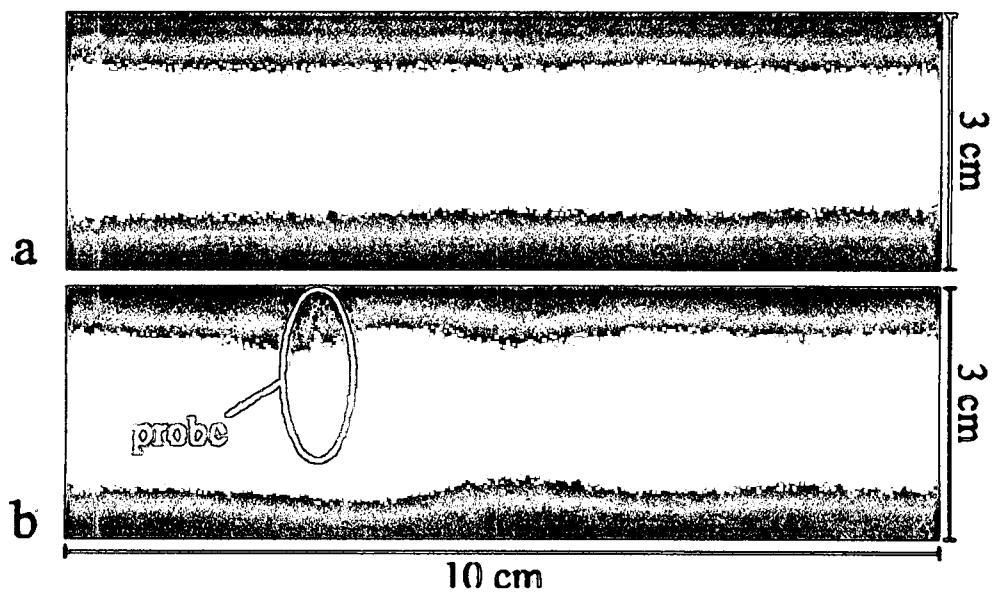


Figure 3: Section of a plasma discharge tube that a probe can be inserted with an undisturbed plasma (a) and a probe disturbed plasma (b)

charge-coupled device (ICCD) plasma imaging, optical emission spectroscopy (including ultraviolet and infrared), and time-of-flight (TOF) analyses.

The objectives of this thesis are as follows: 1) to investigate in situ versus ex situ analyses for three different plasma processes, 2) to correlate material/coating properties to the plasma properties for each process, and 3) to draw conclusions and discuss their impact on materials processing. The outline for achieving these objectives is illustrated in Figure 4. After the introduction, the three types of analysis tools are outlined. The following section introduces each project, and gives background information. Each of the three parallel experimental paths describes the set-up, outlines the experimental procedures, and reviews the results and discussion. A final summary and conclusion section tie the three projects back to the main thesis objectives.

## **1.2 Ex Situ Coating Analysis Tools**

### **1.2.1 X-Ray Photoelectron Spectroscopy**

X-ray photoelectron spectroscopy is used for determining the chemical composition of a coating surface [3]. A monochromatic X-ray source (usually aluminum or magnesium) irradiates a sample under ultra high vacuum (UHV). The X-rays interact with electrons in each element with a specific energy imparting their energy to the electron. If the energy of the incident X-ray is greater than a bound electron's specific binding energy, it may be ejected from the atom. As the electron is leaving the atom, it has a kinetic energy equivalent to the difference between the X-ray energy and the binding energy of that electron. The kinetic energy of the emitted electron is measured

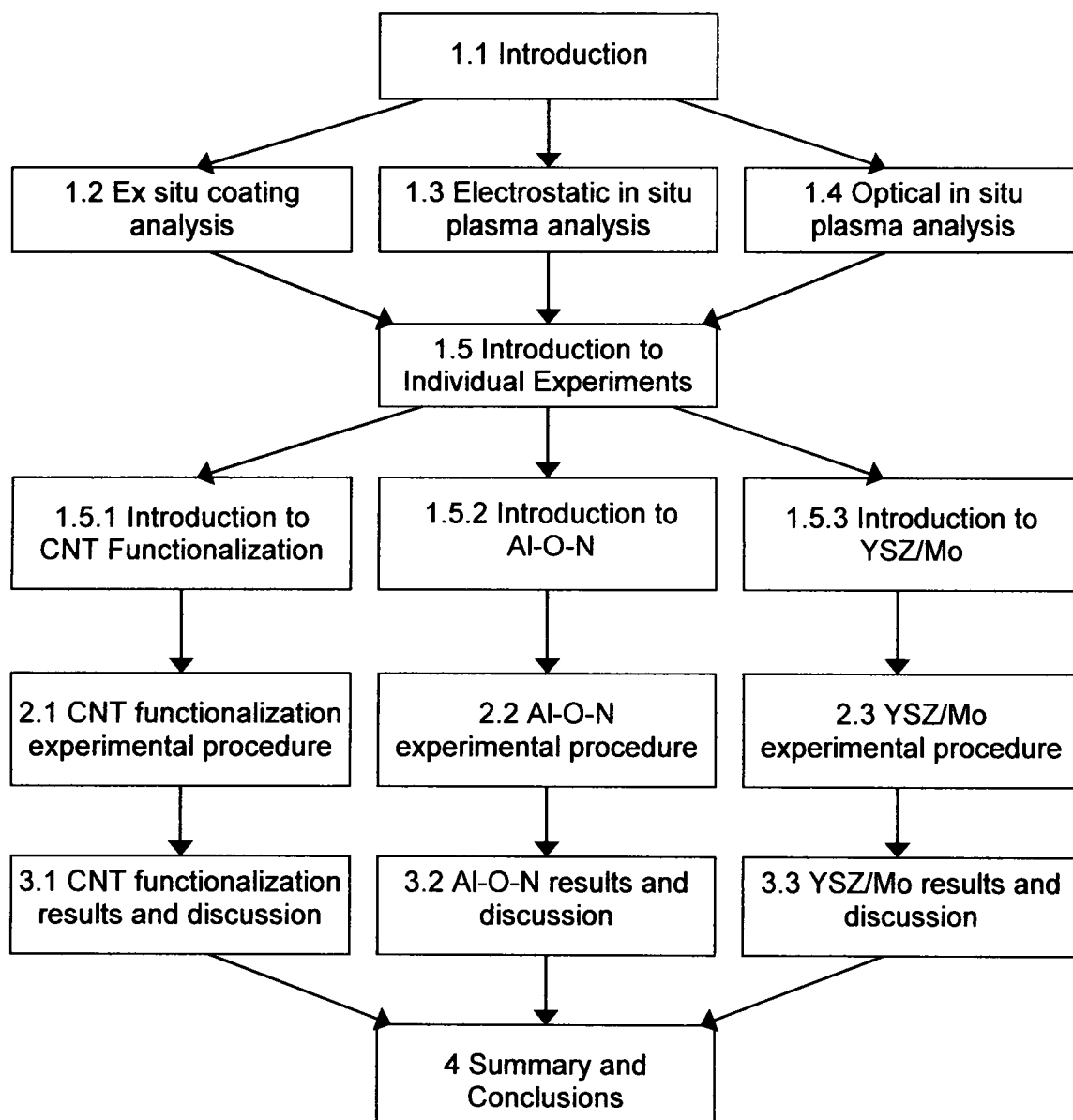


Figure 4: Thesis Overview

by a detector and a peak appears on the scan. Using a database, each peak can be identified by which element and orbital the electron originated. If the XPS system is properly calibrated, atomic compositions accurate to 0.1 atomic percent can be calculated.

### **1.2.2 X-Ray Diffraction**

XRD is a useful technique for determining crystal structure and lattice parameters of a solid coating [4]. A typical XRD scan is called a  $\Theta$ - $2\Theta$  scan. A sample is mounted at a specific angle relative to the x-ray detector and the x-ray source. The angle from the x-ray source is  $\Theta$  and the angle from the x-ray detector is twice  $\Theta$ , or  $2\Theta$ . As the sample is rotated and the angle  $\Theta$  increases, the X-ray detector rotates around an axis in order to maintain its  $2\Theta$  angle. As the sample is rotated over a set  $\Theta$  scan range, monochromatic X-rays (usually from a copper source) bounce off from the sample and scatter. X-rays that strike a specific crystallographic plane will show up as a large peak in the XRD scan. Another technique is a glancing angle X-ray scan. In this scan, the sample and x-ray source are fixed, but the detector still moves. This type of scan is good for thin films as the X-ray penetration depth is minimized. The angle of the X-ray tube to the sample is very shallow, so the X-rays will tend to strike much more of the thin-film surface volume, as opposed to having a high angle and returning information mostly about the substrate. When the  $\Theta$ - $2\Theta$  or glancing angle scan is complete, the peaks can be compared to a diffraction database in order to identify the material and crystallographic structure.

### **1.2.3 Raman Spectroscopy**

Raman spectroscopy is used to study vibrational, rotational, and other low frequency modes in a material [5]. Information from a Raman spectroscopy scan does not indicate which elements are present, but can indicate types of bonds that are present in a coating. It relies on the scattering of light from a monochromatic light source (i.e. a laser) and the emission and absorption of phonons. This excitation effect from the monochromatic light source moves the electron to an elevated vibrational state. These phonons and other excitations that are absorbed or emitted by the laser light result in a shift in the energy of the laser photons which is detected by a spectrometer having a CCD array. Each shifted peak is specific to specific molecular vibrations which allows for analysis and modeling of the expected peaks. Raman spectroscopy will not work on metals, but it works tremendously well on crystalline non-metals.

### **1.2.4 Electron Microscopies**

Electron microscopy techniques such as scanning electron microscopy (SEM) and transmission electron microscopy (TEM) are a useful tool to analyze a coating's surface features [6,7]. Both microscopies are made possible by focusing an electron beam with focusing coils in a vacuum. In a SEM, an electron beam is rastered across the sample in order to eject secondary electrons from the surface which strike a detector creating a signal that can be converted into a digital image. The maximum resolution for a SEM is approximately 1 nanometer (nm). TEM operates under the same electron beam principles except the electron beam is not rastered across a sample and samples are thin enough for electrons to pass through the sample to a CCD detector which creates a digital

image. Instead of depending on secondary electron emission for an image, TEM relies upon beam diffraction. The maximum TEM resolution is less than 1 angstrom with an effective magnification of about 50 million.

### **1.2.5 Ball-on-Flat Tribometer**

A ball-on-flat tribometer is used to test the friction and wear characteristics of a coating. In its simplest form, a circular disk on which a coating was deposited is rotated and a steel ball (or other hard material) with a small applied load is dragged across the surface (Figure 2). A force gauge is attached to the arm that holds the steel ball in order to measure the forces between the coating and steel ball. The coating lifetime can be determined by monitoring the friction coefficient that is calculated from the force gauge. The wear debris and wear scars can be analyzed for failure mechanisms and/or and chemical changes in the coating. Some tribometers are equipped to test samples in varying temperature, pressure, and humidity ranges to examine the coating's performance in the environment in which it was designed to operate.

## **1.3 Electrostatic In Situ Plasma Analysis Tools**

### **1.3.1 Langmuir Probe**

A Langmuir probe is a simple, but very powerful plasma analysis tool. In its simplest form, it is a wire held in the plasma that is biased negatively or positively in order to measure current. By varying the voltage from negative to positive and collecting the current readings a chart can be put together (Figure 5 [8]) in order to calculate the



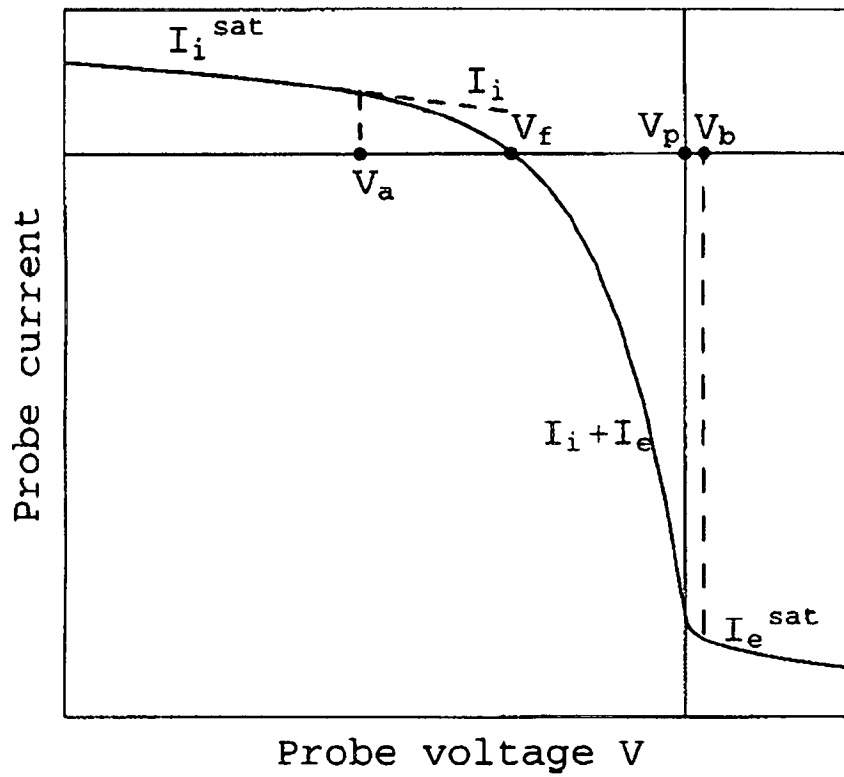


Figure 5: Sample Langmuir Chart

plasma potential, floating potential, sheath potential, electron/ion density, electron temperature, and ion energy [9]. Many of these parameters would be useful for in situ process monitoring, but no tool is without its drawbacks. Although many models predicting how the probe affects the plasma have been published [10,11] a main drawback is still changing the plasma with a probe during a deposition. Another drawback is the noise susceptibility of electrostatic techniques versus optical techniques. Pulsed plasmas are inherently noisier than a steady state plasma process because of the pulse events.

### **1.3.2 Electrostatic Quadrupole Plasma (EQP) Analyzer**

An electrostatic quadrupole plasma (EQP) analyzer can perform many analyses of a stationary plasma. In addition to analyzing mass distributions at specific energies, energy distributions at specific mass/charge ratios can also be analyzed [12]. By analyzing specific points in a plasma, energy and chemistry of all species can be determined. Not only could this help explain the kinetics within the plasma, but it could be used to discover new mechanisms for plasma interaction and coating deposition. Figure 6 [13] is a schematic of an EQP probe. One pair of rods has an applied DC potential while the other pair has a radio frequency (RF) potential that has a matching magnitude of the DC potential, but the DC potential is the opposite sign. Only ions that match a critical DC/RF potential ratio are allowed to pass through the rods to be collected at the other end of the EQP. These ions collected all have the same mass/charge ratio. By varying the potentials, the EQP can scan through a range of mass/charge ratios for a full scan of all plasma species. Besides the disadvantage of having a probe in the

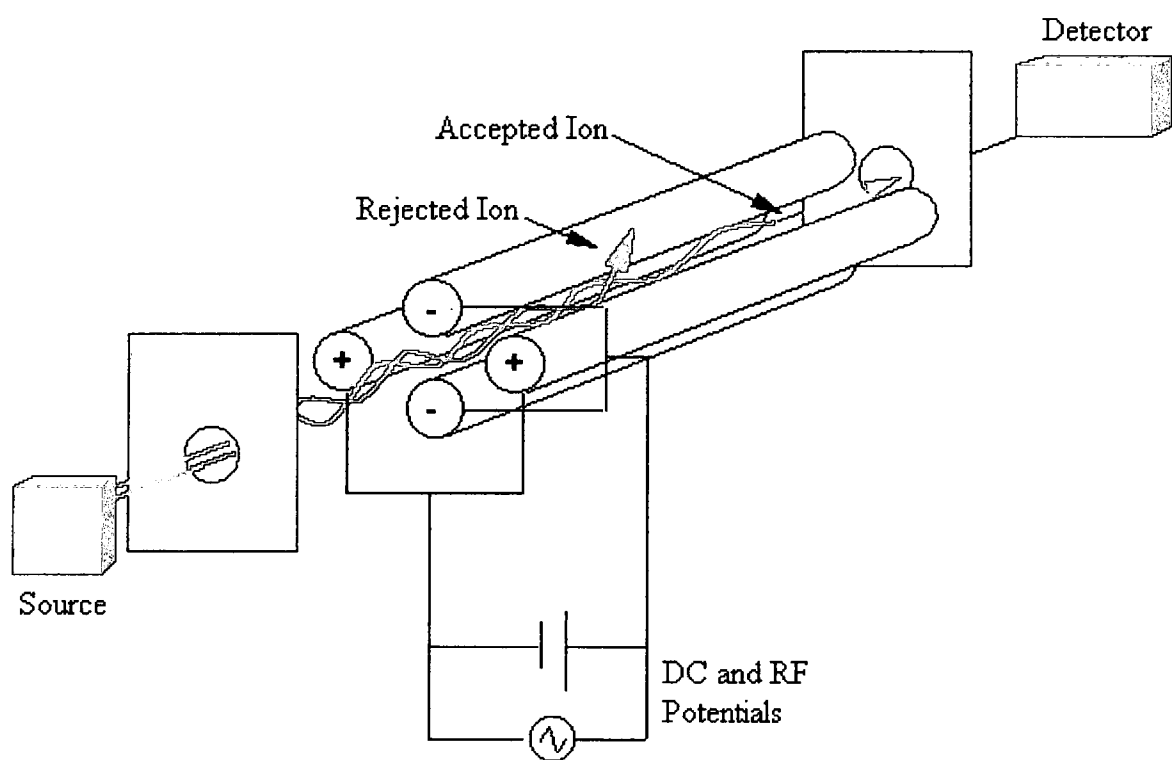


Figure 6: Schematic of an electrostatic quadrupole plasma analyzer

plasma and causing disruptions, the cost of an EQP analyzer is a major drawback. There are many more cost effective and less intrusive methods for monitoring a plasma in an industrial process.

## **1.4 Optical In Situ Plasma Analysis Tools**

### **1.4.1 Intensified Charge-Coupled Device (ICCD) Plasma Imaging**

ICCD plasma imaging is a technique that takes a two dimensional snapshot of a three dimensional plasma. This is a good technique for non-stationary plumes such as those in pulsed laser deposition. Not only does this technique allow for study of plume hydrodynamic phenomena in vacuum and low pressure background gases, but temporal and spatial analysis of plasma species is possible as well. The entire ICCD system would be triggered either by either a photodiode that detects when the laser is fired or by a pulse output signal from the laser. This output signal is received by a programmable pulse generator which triggers a gated image collecting ICCD camera [14]. The ICCD camera itself is fitted with a 35 mm zoom lens to properly focus the image. Narrow band pass optical filters can be fitted to the system in order to take images of specific plume species.

### **1.4.2 Optical Emission Spectroscopy**

Optical emission spectroscopy is one of the simplest and most useful of the optical plasma analysis tools. When a plasma is formed, the electrons in the atoms either jump up to higher energy orbitals or are removed all together from the atom. When these

electrons fall back to a lower energy level or recombine with an ionized atom, the excess energy needs to be released. This energy release is in the form of photons of light at very specific wavelengths for each transition. This light is collected with collection optics coupled to a fiber optic cable and optical emission spectrometer. When the light from the fiber optic cable enters the spectrometer, it strikes a spherical mirror which collimates the light and directs it towards a plane grating. The plane grating diffracts the light which is focused onto a one dimensional CCD array by a second spherical mirror. Through an analog/digital converter, the data is transferred to a computer [15]. The resulting graph shows peaks at each wavelength that is present in the light emitted from plasma. From this peak information, specific species and transitions can be identified.

OES is a qualitative analysis technique, but it can be adapted to be quantitative. Peak intensities for each species are not directly related to the amount of each element or specie present in a plasma. This is due to quantum efficiencies and species mobility in a plasma. If a calibration curve can be made taking into account quantum efficiencies, varying gas concentrations, and changes in pressure, relative quantification of the species in a plasma can be determined.

#### **1.4.3 Time of Flight Analysis**

TOF analysis can be used to analyze a particular species velocity, relative position, and kinetic energy distributions in a plasma [14,16]. To carry out TOF analysis, a photomultiplier tube (PMT), narrow bandpass filters, and a digital phosphorus oscilloscope (DPO) are needed. A collimating tube with a small slit (usually about 1 mm) allows light to pass through a narrow bandpass optical filter (often approximately 10

nm wide) and be collected by a PMT tube. The PMT tube converts and amplifies the signal and sends it to an oscilloscope which collects the waveform. A computer can regularly collect waveforms from the oscilloscope and produce an intensity versus time graph, as well as extract velocity and intensity statistics continuously from the process. TOF analysis is most useful in analyzing non-stationary plasmas, such as laser ablation plumes, with a minimal cost.

## **1.5 Introduction to Individual Experiments**

Each nanostructured material discussed in this thesis has different correlations to be studied. For carbon nanotube functionalization, the relationship between plasma gas mixtures and the degree of surface functionalization was studied for later analysis of tunable tribological properties. The aluminum oxynitride research was performed to explore the relationship between the ion beam and pulsed laser ablation plasmas as they affect coating chemistry and film crystallinity. The yttria stabilized zirconia and molybdenum deposition was studied in order to create a crystalline zirconia nanoparticle and amorphous molybdenum nanocomposite at low temperature and pressure.

### **1.5.1 Introduction to Plasma Functionalization of Carbon Nanotubes**

Since the discovery of carbon nanotubes (CNTs) by Iijima in 1991 [17] the materials science world has been studying CNTs for their unique properties including their strength, thermal conductivity, electrical impedance, and chemical resistance. CNTs are constructed of a 2-D hexagonal array of carbon atoms (a sheet of graphite) rolled into

tubes. Because tube diameters can range from a few angstroms to tens of nanometers, single wall (SWCNT) and multi-wall carbon nanotube (MWCNT) structures are possible. Although CNTs show much promise for future material applications, one major hurdle among many is the functionalization of the outer surface. This is done in order to not only remove unbonded carbon sites, but to enable better mechanical adhesion in composite applications. In this experiment, reactive plasmas of nitrogen/argon and hydrogen/argon mixes were used to functionalize the CNT surface. A later study by Dickrell, et al studied these samples for tunable friction properties [18].

By using pulsed glow discharge plasma at low temperature and pressure, the CNTs can be functionalized without causing major damage to their structure. A pulsed direct current (DC) power supply was chosen for the glow discharge plasma. Regular DC power supplies cannot be used on insulators due to charging, but pulsed DC power supplies ( $>1$  kilohertz) can be used for magnetron sputtering of insulators because their pulses are bipolar. Both a DC and radio frequency (RF) power supply could be used for both conducting and insulating substrates, but the DC system is more flexible. A pulsed DC power supply works by applying a high negative voltage ( $>200$  volts in magnitude) and low current ( $<1$  ampere) across a cathode to create a plasma at the start of a cycle. Negative voltage is applied for a set period of time on the order of microseconds, and then the polarity is switched for a certain reverse time in order to negate any charging effects by positive ions in the cathode. Minimizing the amount of charging also tends to eliminate arcs, which could cause severe damage to the sample. If an arc were to occur, the arc suppression circuitry in the power supply extinguishes them within 5 to 200  $\mu\text{s}$ , thereby eliminating any significant substrate damage.

### 1.5.2 Introduction to IBPLD of Aluminum Oxynitride

Within the last few years, new thin film deposition processes have been developed by utilizing multiple plasma sources. Ion beam pulsed laser deposition (IBPLD) is one of these processes. The IBPLD process involves the intersection at the substrate surface of a pulsed laser ablation plume with an ion beam operating with a gas precursor. These complementary plasma sources combine to successfully control the structure and chemical composition of deposited films. Multiple coatings have been deposited by IBPLD with some of the earliest published work on the growth of yttria stabilized zirconia ( $\text{Y}_2\text{O}_3\text{-ZrO}_2$  or YSZ) and cerium oxide ( $\text{CeO}_2$ ) buffer layers for the growth of epitaxial superconducting YBCO ( $\text{YBa}_2\text{Cu}_3\text{O}_7$ ) films [19]. Other films that have been produced with this method are epitaxial aluminum nitride (AlN) [20], biaxially textured magnesium oxide (MgO) [21], hexagonal boron carbonitride (h-BCN) [22], and fullerene like carbon nitride ( $\text{CN}_x$ ) thin films [23]. What makes this deposition technique so useful is the interaction between the two plasmas. Often this interaction produces additional excited states and plasma chemical reactions that are not present in either plasma alone. This additional energy helps create nanocrystalline phases at lower temperatures in an amorphous matrix [19-23], which in the case of tribology, yields an increase in film hardness and improves wear properties.

In this application of IBPLD, an aluminum oxynitride (AlON) thin film was synthesized. AlON thin films have the potential to have improved thermobarrier, mechanical and dielectric properties over aluminum oxide ( $\text{Al}_2\text{O}_3$ ) and AlN thin films.



The PLD plume was created with an  $\text{Al}_2\text{O}_3$  target, and the ion beam operates in a nitrogen atmosphere to contribute the nitrogen atoms to the coating.

### **1.5.3 Introduction to MSPLD of Yttria Stabilized Zirconia and Molybdenum**

Magnetron sputtering combined with pulsed laser deposition (MSPLD) is another dual plasma source deposition process that has been developed in recent years. This process combines the efficiency of magnetron sputtering of metals with a high energy laser ablation process to deposit oxide materials in order to produce low temperature tribological coatings [24]. Metal or ceramic matrix nanocomposites with multiple embedded materials are a type of coating for which this process is ideally suited. Often these embedded materials are solid lubricants that provide lubrication in different environments and hard nanocrystalline phases to resist coating wear [25]. These composites are often hard to manufacture due to the nature of each of the coating components. The nanocrystalline phase requires higher temperatures to form, but higher temperatures can cause the amorphous metal matrix to crystallize, the substrate material could soften under heating, and other solid lubricants would deteriorate. In this experiment, the magnetron was used to deposit molybdenum (Mo) as the metal matrix and the laser ablation process was used to create the YSZ nanocrystalline phase. In a typical MSPLD set up for a YSZ/Mo coating, the laser and magnetron pulsing are not synchronized, which produces an amorphous film where the metal and oxides are mixed, and the YSZ is not nanocrystalline. The goal of this experiment was to synchronize the laser and magnetron firing so that the higher energies in tandem will allow increased mobility of the deposited atoms but still maintain the required low temperature at the

substrate. This would result in the creation of nanocrystalline YSZ in the amorphous Mo, further increasing the wear resistance of the coating.

## **CHAPTER 2**

### **EXPERIMENTAL PROCEDURES**

#### **2.1 Experimental Procedures for Plasma Functionalization of Carbon Nanotubes**

##### **2.1.1 Carbon Nanotube Sample Treatment**

Vertically aligned MWCNTs were obtained from Rensselaer Polytechnic Institute for surface modification. The surface modification was a reactive plasma treatment process to attach hydrogen and nitrogen atoms to non-fullerene bonded carbons in defect areas in the MWCNT structure for tribological testing. The samples were sequentially treated with the same process, varying only the gas ratios used for each reactive plasma. After the CNT sample was placed on the sample holder, the ultra high vacuum (UHV) chamber was sealed and evacuated to  $10^{-7}$  Torr. Before each sample was plasma treated, each sample was sputter cleaned for 5 seconds at a filament current of 3.5 amperes (A) and a beam voltage of 300 volts (V) with Ar being leaked into the vacuum at 4 standard cubic centimeters per minute (sccm). Prior to the plasma treatment, the chamber was evacuated, and then filled to a pressure of 30 mTorr with gas mixtures consisting of argon as the inert gas and hydrogen or nitrogen as the reactive gas [26]. OES was performed for all gas mixtures listed in Table 1, but only the mixtures with a listed sample number and treatment time were used for treating the CNT samples. The plasma treatment was

Table 1: Carbon nanotube functionalization plasma parameters

<b>Sample</b>	<b>Gas Mixture</b>	<b>Ar Flow Rate</b>	<b>Reactive Gas Flow Rate</b>	<b>Treatment Time (s)</b>
11	Ar/H <sub>2</sub>	0	50	-
	Ar/H <sub>2</sub>	10	40	45
	Ar/H <sub>2</sub>	20	30	-
	Ar/H <sub>2</sub>	30	20	-
12	Ar/H <sub>2</sub>	40	10	45
	Ar/H <sub>2</sub>	50	0	-
	Ar/H <sub>2</sub>			
13	Ar/N <sub>2</sub>	0	50	-
	Ar/N <sub>2</sub>	10	40	45
	Ar/N <sub>2</sub>	20	30	-
	Ar/N <sub>2</sub>	30	20	-
14	Ar/N <sub>2</sub>	40	10	45
15	Ar/N <sub>2</sub>	50	0	45

carried out with an Advanced Energy DC Pinnacle Plus pulsed plasma source set at a nominal voltage of -600 V, a pulse frequency of 150 kilohertz (kHz), and a reverse time of 1 microsecond ( $\mu$ s). The plasma treatment duration for all CNT samples was 45 seconds. The plasma source was directly coupled to the insulated sample stage and holder making it the cathode. The ground for the plasma source was attached to the chamber.

### **2.1.2 Plasma Data Collection**

Spectra of each gas mixture was collected with an Ocean Optics HR4000CG-UV-NIR high resolution spectrometer with a 200-1100 nanometer (nm) range and a 10 micrometer ( $\mu$ m) slit with a fiber optic collection bundle coupled to fixed position focusing optics. The spectrometer was set to collect data at an integration time of 1000 milliseconds (ms), a scan average of 4, and a boxcar of 0. Table 1 contains all inert/reactive gas mixtures studied in the experiment.

### **2.1.3 Functionalized Carbon Nanotube Data Collection**

In situ and ex situ XPS scans were taken of the five treated samples in an ultra high vacuum environment in order to analyze the surface chemistry of the treated CNTs. The in situ XPS scans were performed with a Staib XPS system that was connected to the plasma treatment chamber through a series of interlocks as illustrated in Figure 7. The magnesium X-ray source was operating at 100 watts, and three series of scans were taken of all 5 samples. Each sample was analyzed before treatment, after the 5 second ion beam cleaning, and after the 45 second plasma treatment. Survey scans from 600-0

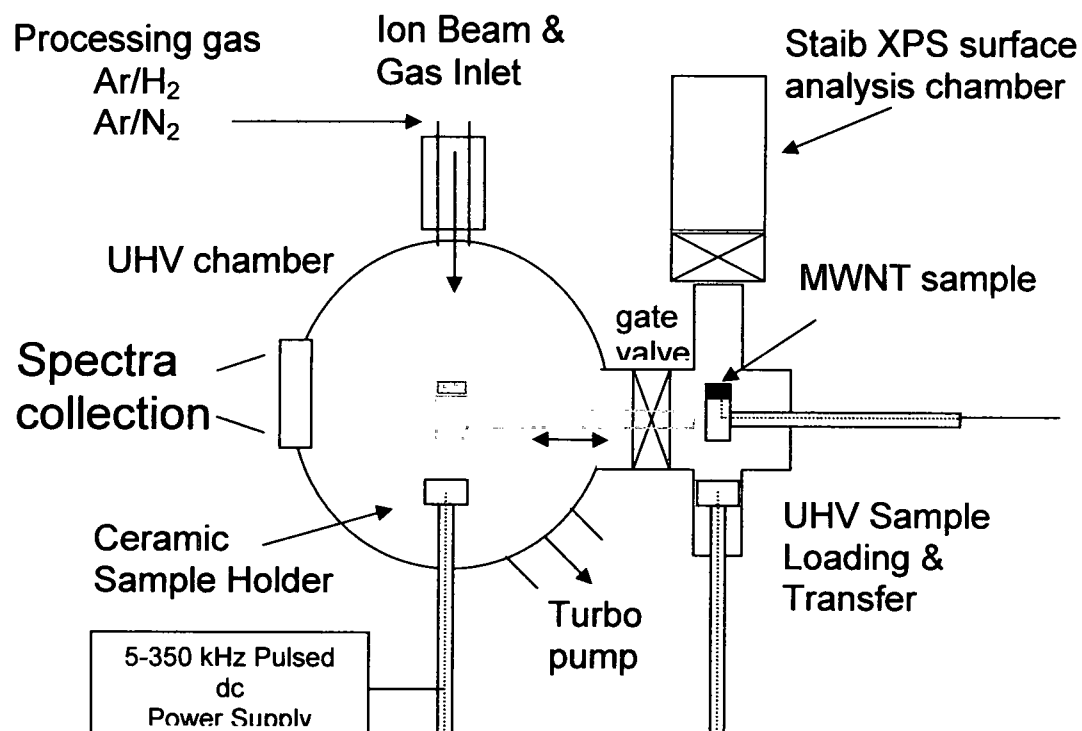


Figure 7: Carbon nanotube functionalization chamber schematic

electron volts (eV) were collected at a 200 ms integration time, a 1 eV step width, and resolution of 3 eV with 10 accumulations. The ex situ XPS used was a Surface Science Instruments M-Probe system operating at 50 watts with an aluminum filament in UHV. This system was used in order to collect high resolution scans of the C 1s peaks. The in situ and ex situ scans can be used to examine the effects of atmospheric exposure to the CNT samples after processing. Usually, the ex situ XPS system would not be used for CNT functionalization analysis, but it was required for higher resolution scans of the C 1s peak. By removing the plasma treated CNT samples from the vacuum system to the ex situ XPS system, a small amount contamination was introduced to the sample surface. This is due to any dangling bonds on the CNT surface which would quickly bond with any oxygen or nitrogen available.

## **2.2 Experimental Procedures for IBPLD of Aluminum Oxynitride**

### **2.2.1 Sample Preparation and Coating Deposition**

Ion beam assisted pulse laser deposition (IAPLD) was used to deposit an Al-O-N thin film coating (Figure 8). The laser used for the deposition was a Lambda Physik COMpex 205 excimer laser (248 nm KrF) with a pulse width of 16 ns at 300 mJ and a repetition rate of 1 Hz. All substrates used were 2.54 cm diameter M50 steel coupons that were heated to 350°C with a heater. A dual UV mirror system with a high speed galvanometer and focusing optics was used to provide uniformly random laser shot dispersion on the Al<sub>2</sub>O<sub>3</sub> (alumina) target at an energy density of 1.5 GW/cm<sup>2</sup>. The alumina target was 8.5 cm away from the substrate at a 45° incidence angle. The ion

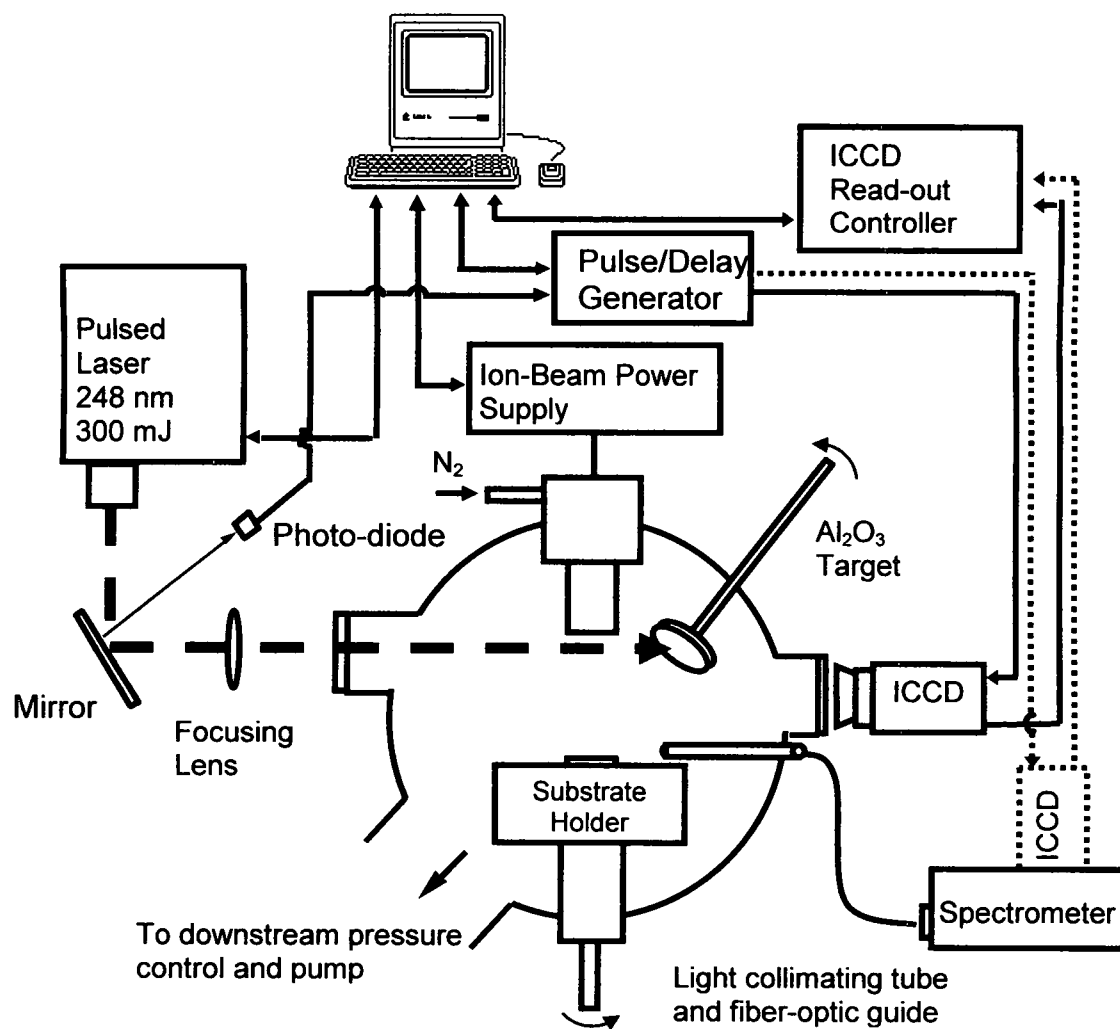


Figure 8: Aluminum oxynitride deposition chamber schematic



beam source used was a 3 cm diameter Kaufman ion beam source (Commonwealth Scientific Group) operating with a high purity N<sub>2</sub> gas precursor at ion energies ranging from 100 to 800 eV. The ion beam focusing grid was positioned 100 mm away from the substrate. Either a -200 V or 0 V substrate bias was applied during coating deposition. All laser parameters were kept constant for all coatings deposited. The process variables were: 1) varying the background N<sub>2</sub> gas pressure from 0.6 to 100 mTorr, 2) ion energy varying from 100 to 800 eV, and 3) bias or no bias on the substrate [27,28]. The central lines for both the ion beam and ablation plume intersected at the substrate center.

### **2.2.2 Plasma Data Collection**

Temporal and spatial plasma distributions were studied with a gated ICCD camera and triggering system as described in section 1.4.1. Two methods of spectral analysis with this system were possible: 1) using narrow band pass filters to take temporal and spatial images of a particular excited species with the ICCD system, and 2) coupling a monochromator and collection optics to the ICCD camera to obtain optical emission spectra. The four narrow band pass filters that were used for temporal and spatial plasma imaging were 280 nm for NO, 391 nm for Al, 780 nm for O, and 820 nm for N. Each filter had a 10 nm bandwidth at FWHM centered on the listed wavelength. The ICCD camera used was a Princeton Instruments 575-S/RBE and the pulse delay generator was a Princeton Instruments PG-200.

OES was performed by coupling the ICCD array used for plasma imaging and a monochromator and adjustable grating as described in section 1.4.2. Like the temporal and spatial analysis, this arrangement allows for triggered and synchronized OES of the

plasmas that can be saved for later analysis. The monochromator attached to the ICCD system was an Acton Research Spectra Pro 150.

### **2.2.3 Coating Data Collection**

XRD and XPS were used to characterize the film chemistry and crystallographic microstructure. A Rigaku-D/max-1B X-ray diffractometer with a Cu K $\alpha$  X-ray source was operated in  $\Theta$ -2 $\Theta$  mode to determine the crystallographic planes present in the samples. The coating surface chemistry was studied by a Surface Science Instruments (SSI) M-probe XPS. The scans were carried out with an Al K $\alpha$  x-ray source plus monochromator with a 25 eV pass energy. Chamber pressure was maintained at about  $3 \times 10^{-9}$  Torr. To compensate for any charging that occurred during the XPS analysis, graphitic carbon at 284.5 eV was used as a reference.

## **2.3 Experimental Procedures for MSPLD of Yttria Stabilized Zirconia and Molybdenum Nanocomposite**

### **2.3.1 Sample Preparation and Coating Deposition**

A hybrid magnetron sputtering and pulsed laser deposition (MSPLD) process (Figure 9) was used to deposit YSZ/Mo nanocomposite thin films. The laser utilized in the process was a Lambda Physik LPX 305i excimer laser (248 nm KrF) with 800 mJ output of 20 ns wide pulses was used to ablate a 5.08 cm (2 inch) diameter YSZ (ZrO<sub>2</sub>/5wt%Y<sub>2</sub>O<sub>3</sub>) laser target. Immediately upon exiting the laser aperture, the beam is

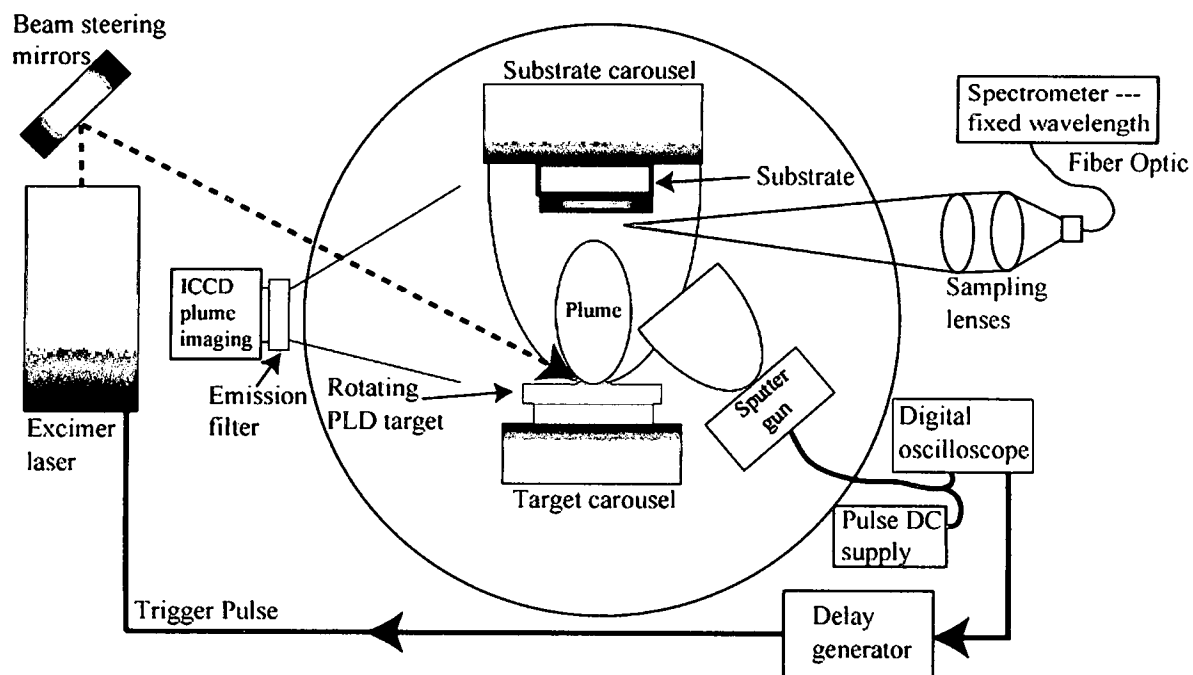


Figure 9: Yttria stabilized zirconia and molybdenum deposition schematic

redirected with a dual UV mirror system that is constantly modulated with a high speed galvanometer to provide uniformly random laser shot dispersion on the YSZ target. After the dual mirror system, the 1 cm x 3 cm beam footprint was focused down to a 1 mm x 3 mm spot using a 500 cm focal length lens. The distance between the laser target and the substrate was 25.4 cm.

The magnetron used for the MSPLD process was a US Gun MiniMak unbalanced magnetron with a 3.175 cm (1.25 inch) diameter Mo cathode. The power supply was an ENI RP650 pulsed DC supply. The distance between the magnetron and substrate was 5 cm. The sample carousel held six 1 inch diameter, 0.25 inch thick 440C stainless steel substrates. The substrates were pre-heated to 200°C with a tungsten filament heater attached to the sample carousel. With the addition of a thermocouple, this temperature was monitored and maintained by the heater system. Power demand to maintain the set temperature decreased due to the thermal heating from the ablation processes. One sample coating was deposited at a time; with the other five samples blanked off from the magnetron and laser plumes. In order to synchronize the two processes, a Tektronix P5200 high-voltage differential probe and a TDS 540D Tektronix digital phosphorous oscilloscope (DPO) were used to measure the voltage from the magnetron in situ. To measure the sputtering current, a Tektronix current probe was clamped around the magnetron power feed line. The DPO was configured to generate a digital trigger based solely on the pulsed sputtering voltage waveform, so that there could be process synchronization. The trigger point was set to the point at which the sputtering voltage rapidly changes from negative to positive. This output trigger was then used as the input into a DG535 Stanford Research digital delay generator. The delay generator was set to

have two parallel output channels. The first channel was for the excimer laser's external trigger input in order to vary the delay time between the magnetron firing and the laser firing. These delays ranged from a 0  $\mu$ s to 10  $\mu$ s delay. The second channel was set to a delay of 33.3 ms, so the laser would fire at a certain time after the magnetron trigger. All depositions took place in a UHV chamber backfilled to a 30 mTorr Ar atmosphere, at 800 mJ laser energy, 30 Hz repetition rate, a substrate bias of -150 V, a magnetron frequency of 120 kHz at 30 W, and a substrate temperature of 200°C [29].

### **2.3.2 Plasma Data Collection**

A two pronged approach was utilized to analyze the plasma created by the MSPLD process: 1) TOF and 2) gated ICCD imaging. TOF analysis was performed with a photomultiplier tube (PMT) and DPO as described in section 1.4.3. Narrow bandpass filters (10 nm) were used to focus on specific excited species in the plasma plume. The two filters used were 470 nm for excited zirconium ( $Zr^*$ ) and 480 nm for excited zirconia ( $ZrO^*$ ) [30]. Voltage and current analysis from the MS was performed by collecting the waveforms on a DPO with a current probe and a high voltage differential probe. This was accomplished during the coating deposition process. Temporal and spatial plasma distributions were studied by a gated ICCD camera and triggering system as described in section 1.4.1. The specific equipment used is listed as follows: a Princeton Instruments 575-S/RBE ICCD imaging camera, a Princeton Instruments PG-200 delay generator, Tektronix TDS 540 D digital phosphorus oscilloscope, and a Tektronix P5200 high-voltage differential probe.

### **2.3.3 Coating Data Collection**

Analyses of coating properties were performed using a Rigaku Rotaflex X-ray Diffractometer (XRD) and a Surface Science Instruments M-Probe X-ray photoelectron spectrometer (XPS). The XRD analysis was performed using glancing incidence X-rays from a Cu X-ray source operating at 6 kilowatts (kW) with a fixed value of  $4^\circ$  for  $\theta$ . Immediately before XPS analysis, the samples were sputtered clean for 15 seconds with 5000 eV  $\text{Ar}^+$  ions. The XPS analysis was performed with an aluminum X-ray source operating at 50 W. From the XPS analysis, the relative peak heights were measured to obtain the composition of each atomic element in the nanocomposite coating.

## CHAPTER 3

### RESULTS AND DISCUSSION

#### 3.1 Analysis and Discussion of Plasma Functionalization of Carbon Nanotubes

##### 3.1.1 Plasma Diagnostics Analysis

Figures 10 and 11 show all spectra as outlined in Table 1 for the hydrogen/argon and nitrogen/argon plasmas, respectively. The only two hydrogen peaks that appear in the wavelengths examined for all plasmas are at 656.3 and 486.1 nm. These peaks are both excited monatomic hydrogen species ( $H^*$ ). In the 80% hydrogen and 20% argon plasma, the  $H^*$  peak intensities are at their maximum. From this point, as the argon concentration was increased and the hydrogen content dropped, the hydrogen peaks both linearly decreased in intensity. Conversely, as argon is added, all excited argon species ( $Ar^*$ ) experience a linear increase in intensity. The nitrogen/argon plasmas reacted differently from the hydrogen/argon plasmas. The 100% nitrogen plasma contained a large distribution of monatomic and diatomic species. The predominant species were excited nitrogen gas (1<sup>st</sup> and 2<sup>nd</sup> positive,  $N_2^*$ ), excited monatomic nitrogen ( $N^*$ ), and singly ionized monatomic nitrogen ( $N^+$ ). As the nitrogen content in the plasma decreased, the intensities of all nitrogen peaks decreased as well. Each subsequent

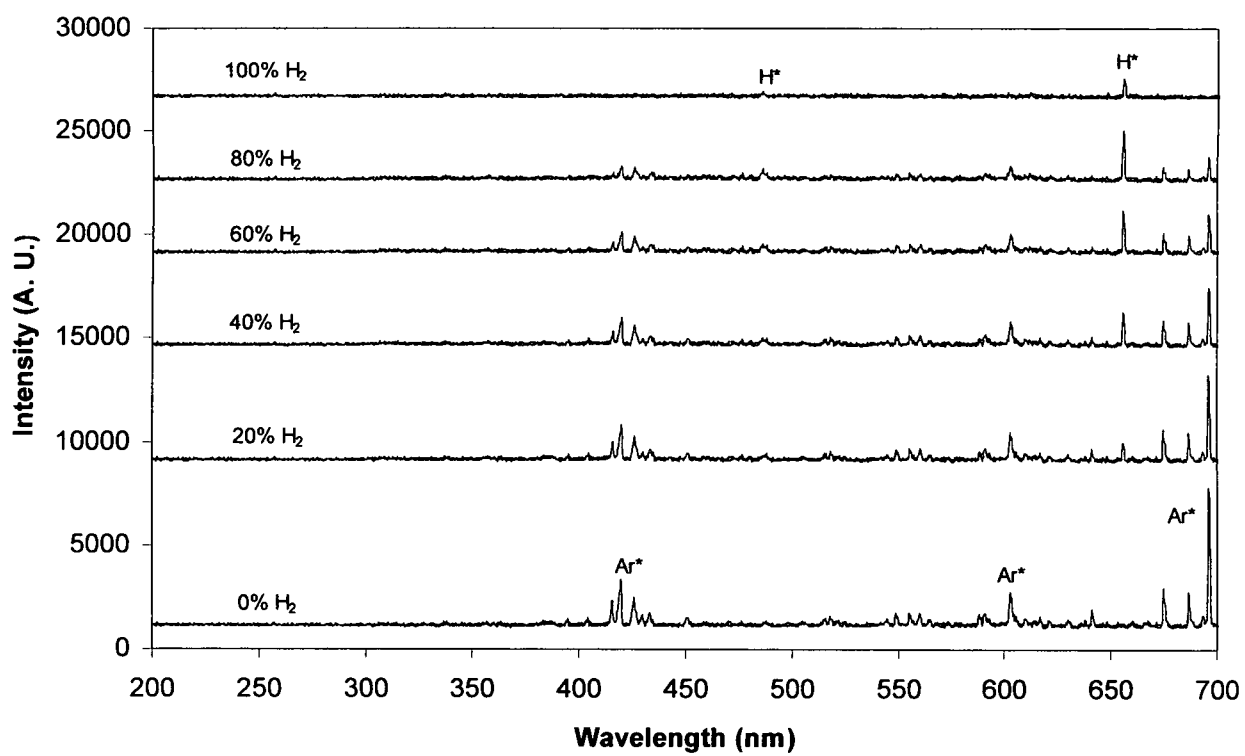


Figure 10: OES for all H<sub>2</sub>/Ar plasma gas mixtures



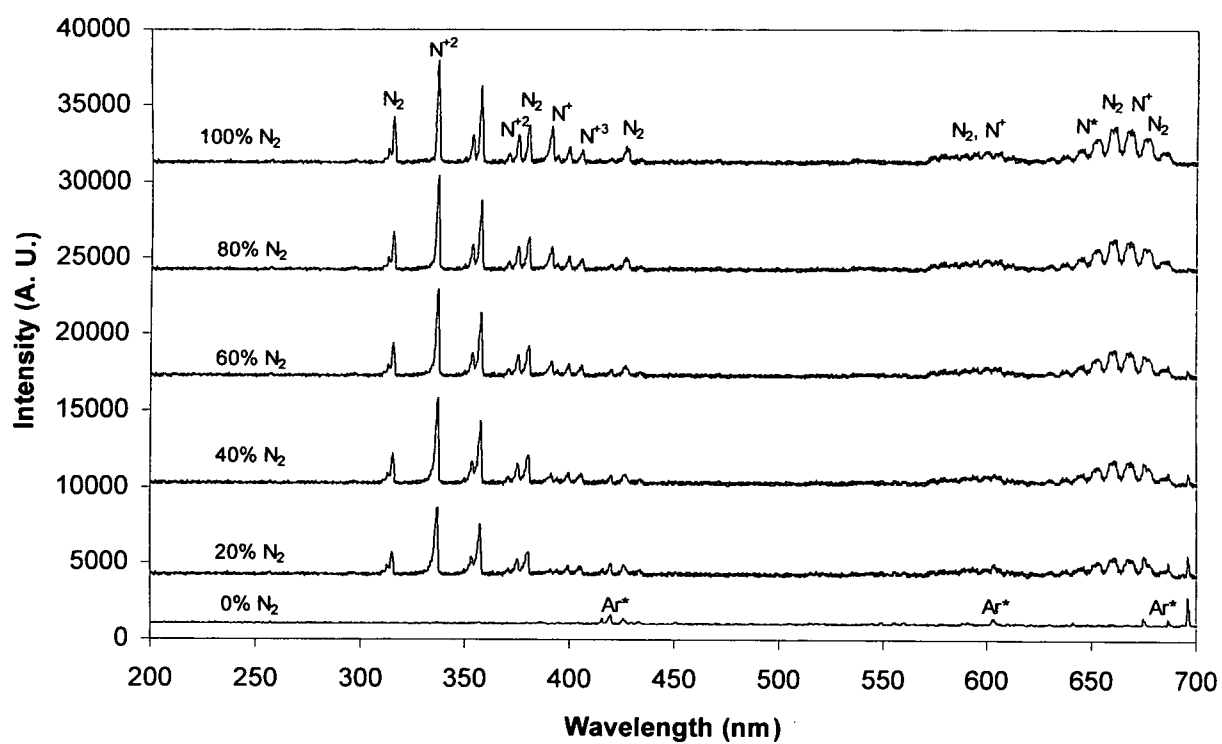


Figure 11: OES for all  $N_2/Ar$  plasma gas mixtures

plasma of lower nitrogen content did not yield linear decreases for all peaks. Most of the peaks maintain a large percentage of their full intensities down to 20% nitrogen. The peak that appears to be affected the most is the  $N^+$  peak at 391 nm. It is non-existent at 20% nitrogen, but grows much quicker than all the other peaks with increasing nitrogen gas content in the plasma. As in the hydrogen plasma, all argon peaks are  $Ar^*$  and they all increase intensities linearly with increasing argon gas content. Further details of each detected specie and its corresponding transition are listed in Table 2 [30-36].

### 3.1.2 Coatings Analysis

In situ XPS was used to minimize sample contamination that would occur in bringing the treated samples back to atmospheric pressure from vacuum and transferring to a stand alone XPS system. While this contamination could be minimized by using an ion beam source to clean the surface of the sample in an ex situ analysis system, it was decided that in doing so, the ion beam itself would modify or damage the sample. Figures 12, 13, and 14 show the XPS results from the preliminary survey scan before any treatment, after the sample was cleaned with the argon ion beam, and after the sample was plasma treated, respectively. The intensities of each scan differ due to different chamber pressures in the XPS analysis chamber. The C 1s peak and its other scan features dominate each scan, but a few scans from Figures 12 and 13 show varying degrees of oxygen and nitrogen contamination as evidenced by the small O 1s peaks shown at 532 eV and the very low intensity N 1s peaks at 399 eV [37]. Figure 14 also shows oxygen contamination in all scans as well as nitrogen contamination in the Ar and Ar/H<sub>2</sub> treatments. The source of this contamination will be discussed in the next section.

Table 2: All identified OES plasma species in carbon nanotube functionalization plasmas

Specie	Transition	Wavelength (nm)
N2 (2nd pos)	$C^3\Pi_u - B^3\Pi_g$	307-316
N2 (2nd pos)	$C^3\Pi_u - B^3\Pi_g$	315.4
N III	$4P^o - 4P$	336.734
N2 II	$B^2\Sigma_h^+ - X^2\Sigma_g^+$	353.9
N2 II	$B^2\Sigma_h^+ - X^2\Sigma_g^+$	358
N2 (2nd pos)	$C^3\Pi_u - B^3\Pi_g$	370-380
N IV	$1P^o - 1D$	374.754
N2 (2nd pos)	$C^3\Pi_u - B^3\Pi_g$	380
N II	$1P - 1P^o$	391.9
N II	$1P^o - 1D$	399.5
N IV	$1P^o - 1D$	405.776
Ar I	$2[3/2]^o - 2[3/2]$	415.859
Ar I	$2[3/2]^o - 2[1/2]$	419.8317
Ar I	$2[1/2]^o - 2[1/2]$	425.9362
N2 (2nd pos)	$C^3\Pi_u - B^3\Pi_g$	427
Ar I	$2[1/2]^o - 2[3/2]$	433.3561
H I	$2p^o - 2D$	434.047
Ar II	$2p - 2p^o$	476.4865
H I	$2p^o - 2D$	486.133
N II	$1P^o - 3D$	574.73
N2 (1st pos)	$B^3\Pi_g - A^3\Sigma_u^+$	536-612
N II	$3P - 3D^o$	592.781
N II	$3P - 3D^o$	595.239
N I	$2S^o - 2P$	599.943
Ar I	$2[3/2] - 2[1/2]^o$	602.515
Ar I	$2[5/2] - 2[7/2]^o$	603.2127
N2 (1st pos)	$B^3\Pi_g - A^3\Sigma_u^+$	630-690
Ar I	$2[1/2] - 2[3/2]^o$	641.6307
N III	$4P - 4D^o$	646.702
H I	$2p^o - 2D$	656.2852
N II	$1D - 1F^o$	661.056
Ar I	$2[1/2] - 2[3/2]^o$	675.2834
Ar I	$2[1/2] - 2[1/2]^o$	687.1289
Ar I	$2[3/2]^o - 2[1/2]$	696.5431

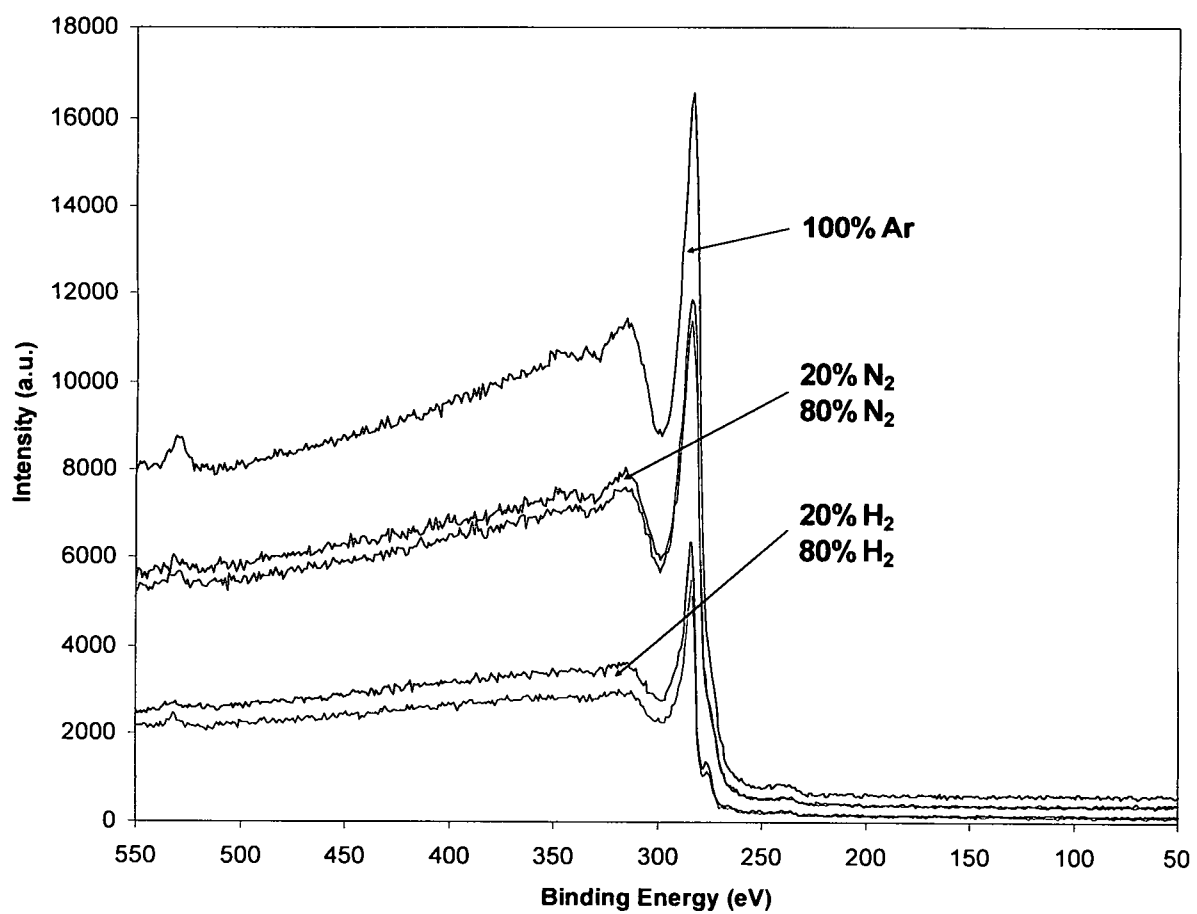


Figure 12: As received XPS scans of carbon nanotube samples

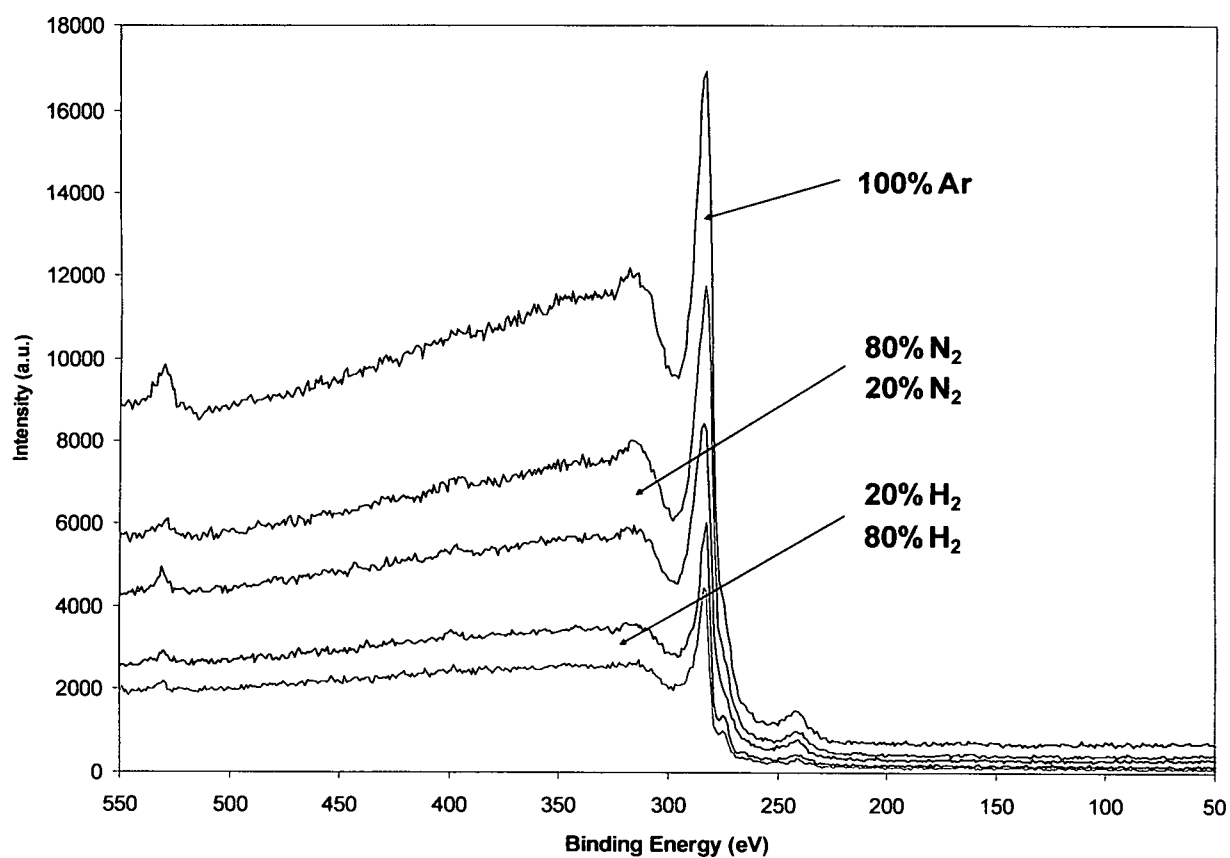


Figure 13: XPS scans of carbon nanotube samples after 5 second plasma cleaning

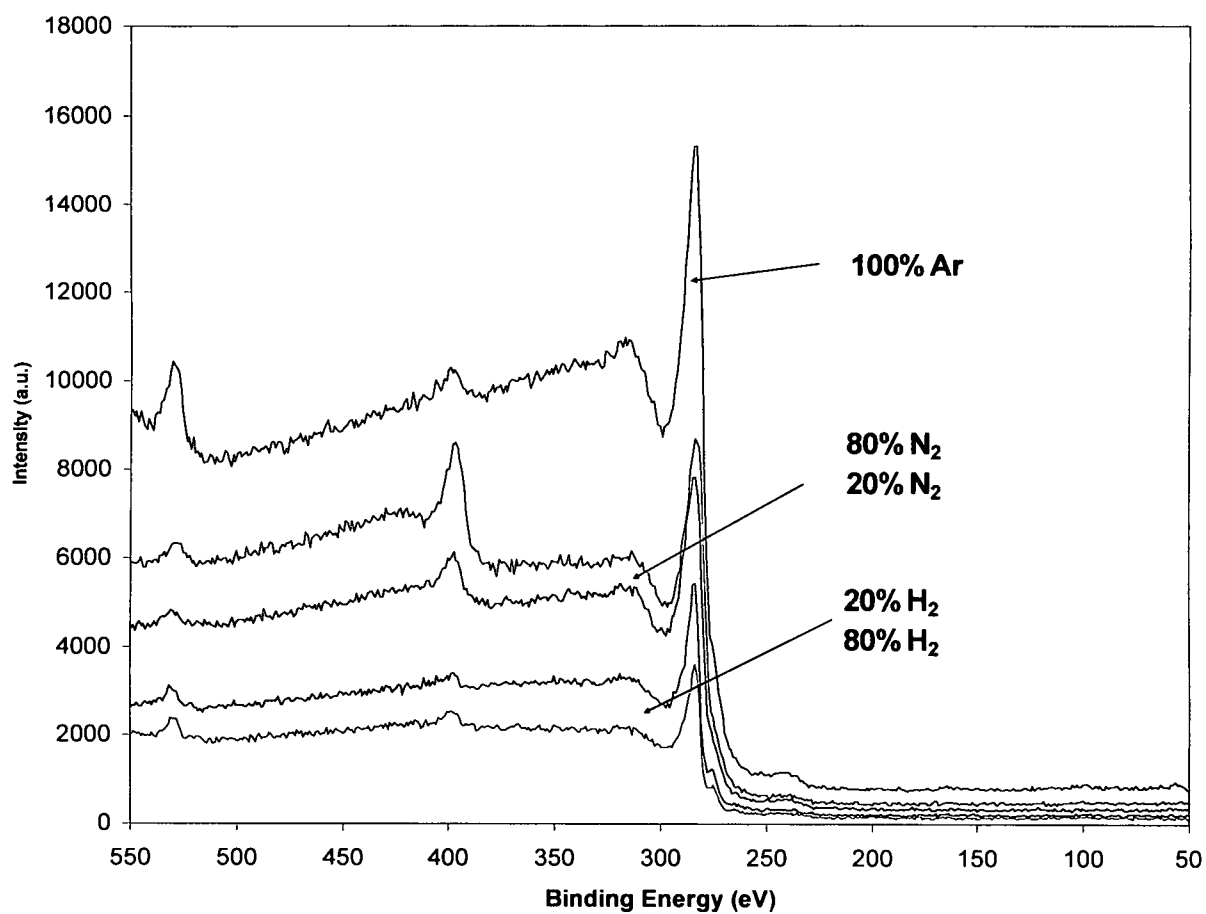


Figure 14: XPS scans of carbon nanotube samples after 45 second plasma treatment

The 5 second argon ion beam treatment that occurred between Figures 12 and 13 did little to modify the CNT surface, and subsequently had little or no change in the XPS results. Figure 14 illustrates the final results of the plasma treatment as outlined in section 2.1.1. The 100% argon scan shows small oxygen and nitrogen contamination peaks, but is otherwise unchanged. Both the nitrogen/argon plasma treated samples show a large incorporation of nitrogen into the carbon nanotubes. As expected, the higher nitrogen content plasma (80% nitrogen/20% argon) resulted in a larger amount of nitrogen incorporation in the CNT sample. The survey scans of the hydrogen/argon plasmas resulted in only the contamination peaks, because hydrogen does not show up on XPS scans. In this case, the hydrogen can only be indirectly detected in high resolution scans of the carbons peaks by a slight bonding energy shift in the deconvoluted peak C 1s peak.

Figure 15 shows three C 1s high resolution XPS scans from the ex situ system. The first scan is of the original untreated MWCNT surface, the second scan is of the 20% hydrogen/80% argon plasma treatment samples, and the third scan is of the 20% nitrogen/80% argon plasma treatments. Figure 15a shows that the untreated CNT samples were nearly pure as the C 1s peak at 284.5 nm cannot be deconvoluted into multiple peaks. The carbon peak for the 20% hydrogen/80% argon plasma treated sample can be separated into two separate peaks which are marked as blue in Figure 15b. The shorter of the two peaks is identified as the C-H bond at 285 eV [37]. The taller peak is the C-C bond at approximately 284.5 eV, which in good agreement with literature values [37,38]. In the 20% nitrogen/80% argon plasma treatment high resolution scan, the C-C bond and two additional peaks appear after deconvoluting the C 1s peak. The main

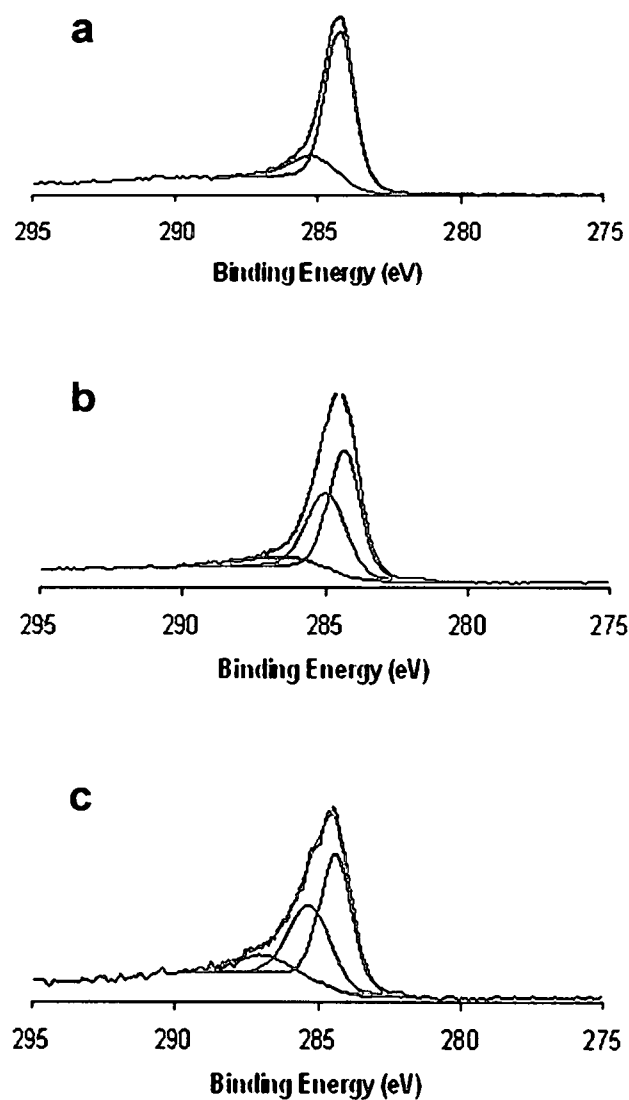


Figure 15: High resolution XPS scans of carbon nanotube C 1s peak - as received sample (a), sample after 45 second 20% H<sub>2</sub>/80% Ar plasma treatment (b), and sample after 45 second 20% N<sub>2</sub>/80% Ar plasma treatment (c)



C-C peak is again at approximately 284.5 eV, and the two additional peaks match the range for C-N and C=N bonding at 287.23 eV and 286.2 eV, respectively [37]. Because of the widening of the C peak, these high resolution XPS scans indicate that the nitrogen and hydrogen are not merely being implanted in the sample, but are actually bonding to the CNTs.

### 3.1.3 Discussion

Among many correlations that can be made between the plasma treatment process and the resulting changes to the CNTs is the amount of damage to the CNT structure. Figure 16a is the SEM of a CNT sample before any treatment. It shows a uniform surface morphology without any damage. Figures 16b and 16c show the surface damage from the 80% nitrogen and 20 % nitrogen plasma treatments, respectively. There is damage to the surface of both samples, but the 80% nitrogen plasma treatment sample has extensive clumping and deep etch wells on the surface. The 20% nitrogen plasma sample shows smaller clumps, fewer deep etch wells, and small fibrous strands. The clumps and fibrous structures are most likely fused bundles of CNTs mixed with carbon structures that are deformed or damaged nanotubes. Figures 16d and 16e show much less surface morphology damage from the 80% hydrogen and 20% hydrogen plasma treatments. The 20% hydrogen plasma treatment sample appears to have little or no damage. The small amount of damage from the 80% hydrogen plasma treatment sample is limited to a small amount of etching, but none of the large clumps or fibrous structures observed in the nitrogen plasma treatment samples. This would be expected as

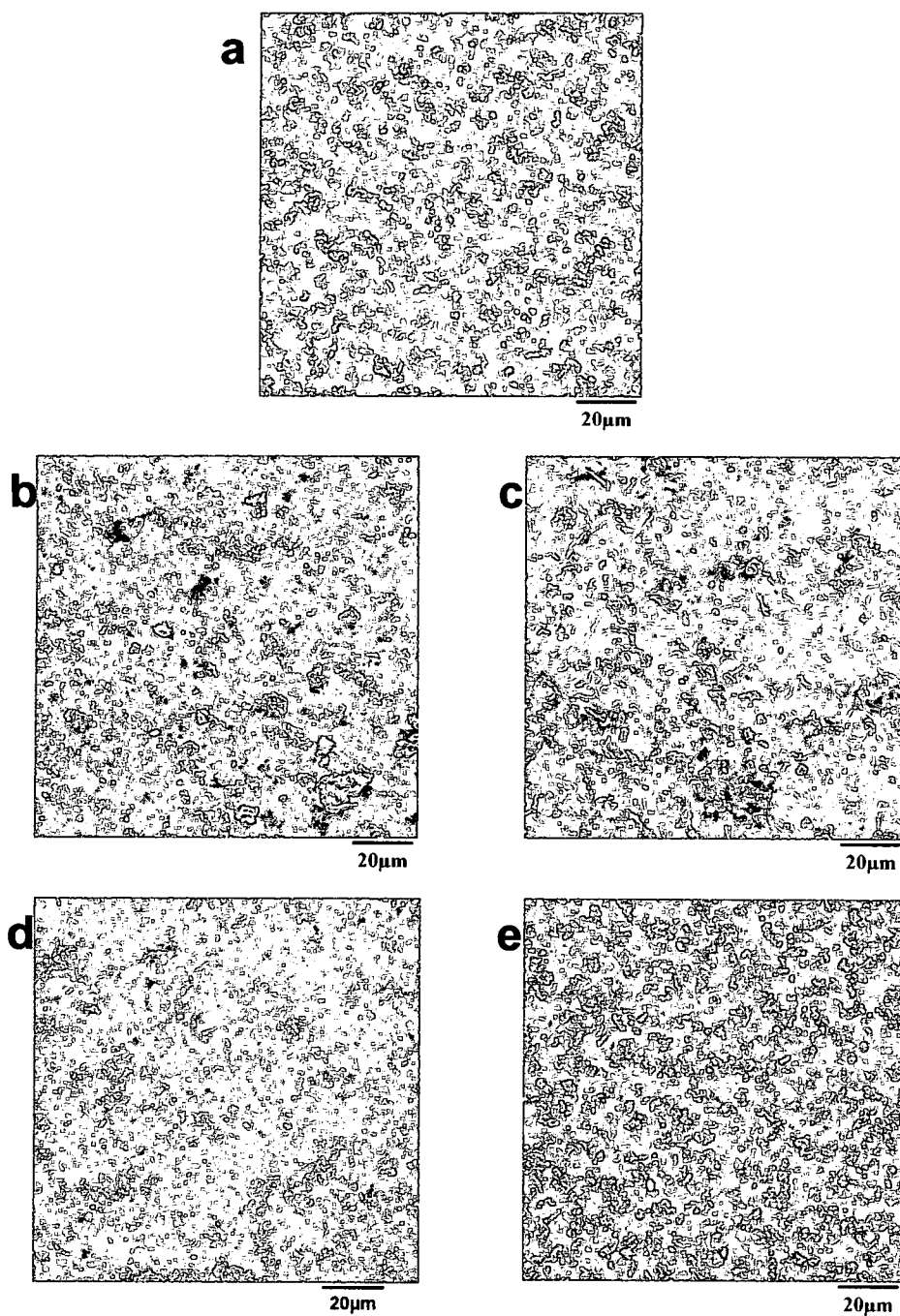


Figure 16: Carbon nanotube SEM micrographs of as received sample (a), 80% N<sub>2</sub>/20% Ar plasma (b), 20% N<sub>2</sub>/80% Ar plasma (c), 80% H<sub>2</sub>/20% Ar plasma (d), and 20% H<sub>2</sub>/80% Ar plasma (e)

nitrogen/argon plasmas are much more energetic than hydrogen/argon plasmas. This is illustrated in Figures 10 and 11. The nitrogen plasma has over ten times the number of optically emitting species in its plasma compared to the hydrogen plasma. Also, the nitrogen plasmas had higher energy species present such as  $N^*$ ,  $Ar^*$ ,  $N^+$ ,  $N^{+2}$ ,  $N^{+3}$ , and  $N_2^+$  while in the hydrogen plasmas, only  $H^*$  and  $Ar^*$  was detected. These two factors indicate that the higher concentrations of excited and ionized species will cause more surface morphology damage.

A comparison between the XPS chemical analysis and the plasma spectroscopy reveals more about the degree of CNT functionalization. The nitrogen plasmas showed only monotonic increases in intensity for most species and almost no change in the species diversity (besides the previously mentioned  $N^+$  peak at 391 nm and Ar species) in the plasma from 20% nitrogen to 100% nitrogen. From this data, one would assume that the amount of nitrogen incorporated in the sample would be approximately the same. This is a false assumption as Figure 14 shows the 80% nitrogen plasma treatment sample has a peak three times as large as the 20% nitrogen plasma treatment. The key to the increase in functionalization is the  $N^+$  specie at 391 nm. Higher energy ions such as  $N^{+2}$  and  $N^{+3}$  are too short lived in a plasma due to their high energies and the elevated amount of free electrons.  $N_2^+$  ions travel across a plasma sheath and arrive at a biased surface with only a fraction of the applied bias energy.  $N^+$  species arrive at a biased substrate with nearly all of the bias energy; in this case -600 V [39]. By arriving at the substrate with higher energy, the ions are able to cause more damage to the CNT surface. It is also possible that the N species responsible for functionalization of the CNTs might be outside the range analyzed by the spectrometer. The hydrogen treatments are a little harder to

interpret. Since hydrogen is not detectable with XPS, the only evidence that there are and C-H bonds in the sample is through interpretation of the C 1s peak. As seen in Figure 15b, the C 1s peak is wider which hints at bonding other than carbon to carbon. The deconvoluted peak shows there are indeed two peaks, which as mentioned earlier, match literature values for C-C and C-H bonding.

As previously mentioned, small nitrogen and oxygen contamination peaks appear in Figures 12, 13, and 14. These contaminants come from two different sources: 1) absorbed water vapor on the surface of the CNTs and 2) oxygen and nitrogen absorbed between the CNTs. The oxygen contamination peaks in Figure 12 are a result of water vapor from the ambient air that was absorbed while the CNTs were stored at ambient conditions. Although an O plasma was used to clean the samples after the CVD deposition process [18], the as received sample (Figure 15a) showed no C 1s peak widening that would indicate oxygen bonded to carbon. If there were C-O bonds, a small peak from 286.1 eV to 286.8 eV would be seen. The CVD process used only ferrocene, xylene, and an argon carrier gas to grow the CNTs, all of which contain no oxygen. Assuming the chamber had no major leaks, the most likely hypothesis is that water vapor absorbed from the air is the source of the oxygen. The oxygen and nitrogen contamination that appears in Figures 13 and 14 are from absorbed gasses on the CNT walls. Preliminary data as yet to be published involving the heating and outgassing of MWCNTs on Inconel is shown in Figure 17 [40]. With a linear heating rate of approximately 7.5°C/min, Figure 17 shows that the CNT walls absorb gasses from the atmosphere, possibly on the interior walls of the multi-walled structure. As the temperature was raised, this gas desorbs from the CNT sample. Looking back at

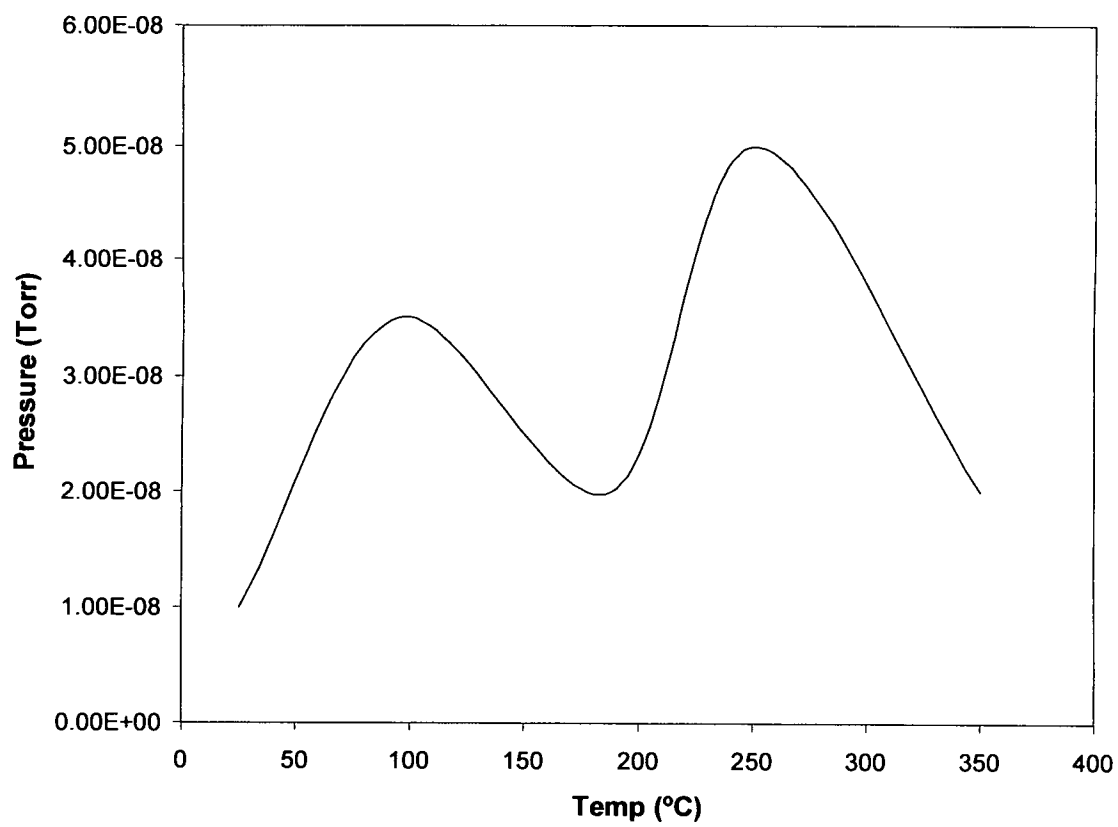


Figure 17: Temperature vs. chamber pressure in the outgassing of a carbon nanotube sample on Inconel

Figure 13, the 5 second ion beam treatment in argon added a small amount of heating to the sample, which allowed some of the gasses to desorb. Couple this gas desorption to the damage caused by ion beam bombardment of the CNTs and the result is that the unsaturated carbons bond to the oxygen and nitrogen. This could explain the small increase in both oxygen and nitrogen content in the samples. In Figure 14, this effect is even more evident with the 45 second plasma treatment. Greater heating occurs which releases more trapped gasses. At the same time, the longer duration and higher energy create more broken C-C bonds, resulting in higher nitrogen and oxygen incorporation. It is also worth noting that even without ion beam bombardment, at  $1.0 \times 10^{-8}$  Torr the gas flux is still approximately  $4 \times 10^{12}$  atoms per  $\text{cm}^2$  second as predicted by the Hertz-Knudsen equation for molecular flux. This would also contribute to a small amount of contamination.

By removing the plasma treated CNT samples from the vacuum system to the ex situ XPS system, a small amount contamination was introduced to the sample surface. This is due to any unsatisfied bonds on the CNT surface which would quickly bond with any O or N available. This would be a small amount of contamination compared to the nitrogen and hydrogen already incorporated into the sample. Figures 15b and 15c illustrate this point as neither scan contains a C-O deconvoluted peak from 286.1 eV to 286.8 eV.

A paper from Khare, et al on nitrogen plasma functionalization of CNTs studied the relationship between the remote plasma source distance from the CNT substrate and the degree of functionalization [41]. Samples that were placed seven cm from the plasma source showed no functionalization. As distance between the plasma source and the

sample was dropped to 1 cm, higher energy bonds began to form, illustrating a clear correlation between more energetic species and having the CNT samples at a shorter distance. With our experimental set up, the effective distance between the plasma source and the sample is zero; our sample is the cathode. This would explain both the large degree of damage to the CNT surface morphology and the higher energy bonding between the CNTs and the incorporated nitrogen.

### **3.2 Analysis and Discussion of IBPLD of Aluminum Oxynitride**

#### **3.2.1 Plasma Diagnostics Analysis**

Coupling of the ICCD system to the monochromator and triggered OES with a 2 nanosecond resolved time scale made it possible to analyze the ion beam, the pulsed laser ablation plume, and the interaction of the two plasmas. Figure 18 shows each separate plasma spectra. In the PLD plume, the only species detected were excited aluminum ( $\text{Al}^*$ ) and excited oxygen ( $\text{O}^*$ ), but no aluminum oxide or ionized species. The main nitrogen ion beam species were excited nitrogen gas ( $\text{N}_2^*$ ), ionized diatomic nitrogen gas ( $\text{N}_2^+$ ), excited monatomic nitrogen ( $\text{N}^*$ ), and singly ionized monatomic nitrogen ( $\text{N}^+$ ). The coupled plasma sources yielded new emission bands that were not present when each plasma source was operated alone. In addition to excited and ionized O and N species, NO species were also detected. These NO species resulted from  $\text{A}^2\Sigma^+ \rightarrow \text{X}^2\Pi$  and  $\text{B}^2\Pi \rightarrow \text{X}^2\Pi$  transitions. Table 3 [42,43] lists in detail each detected specie, its corresponding transition, and in which plasma it was detected.

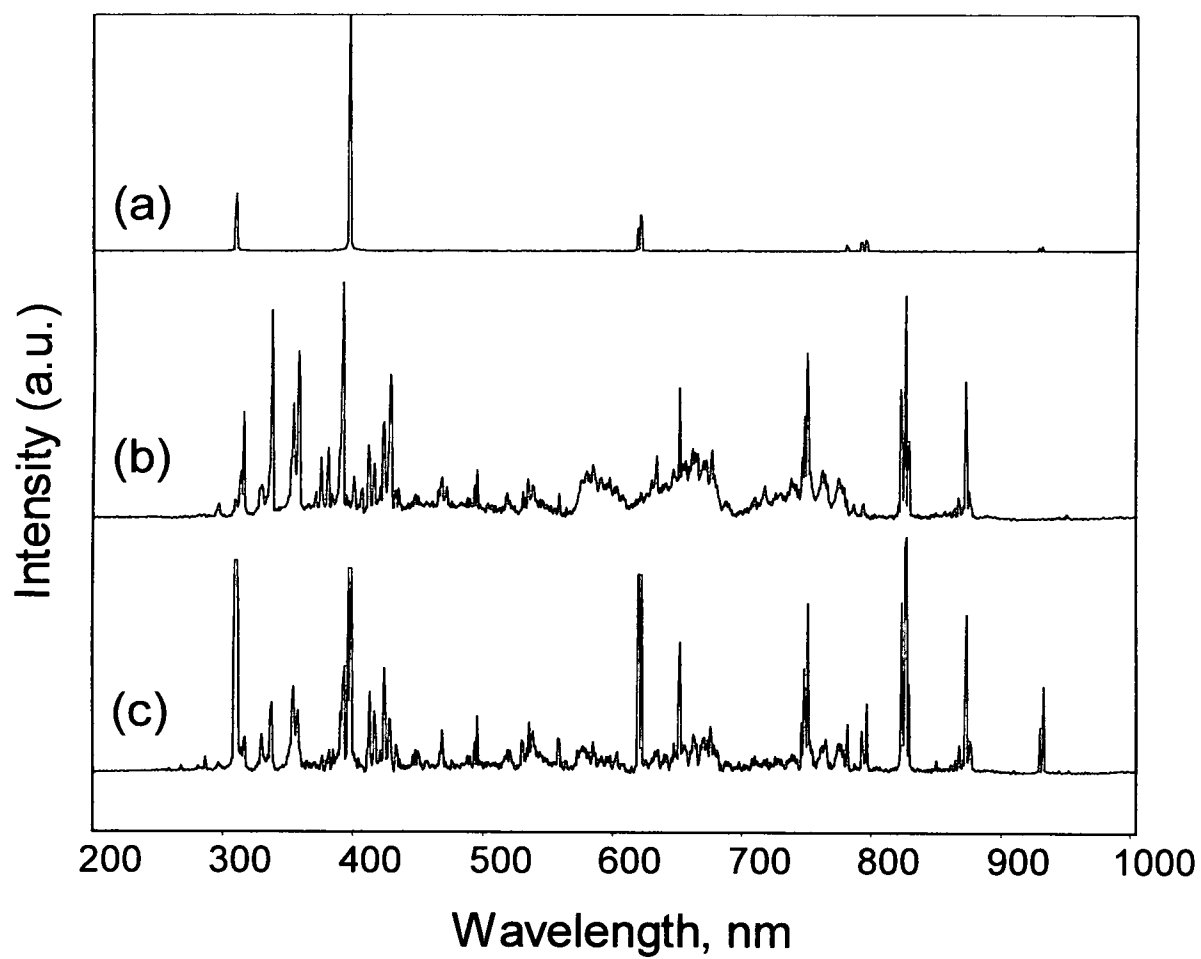


Figure 18: OES spectra from IBPLD process - PLD of Al (a), Ion beam with N<sub>2</sub> gas (b), and combined PLD of Al and ion beam in N<sub>2</sub> gas (c)



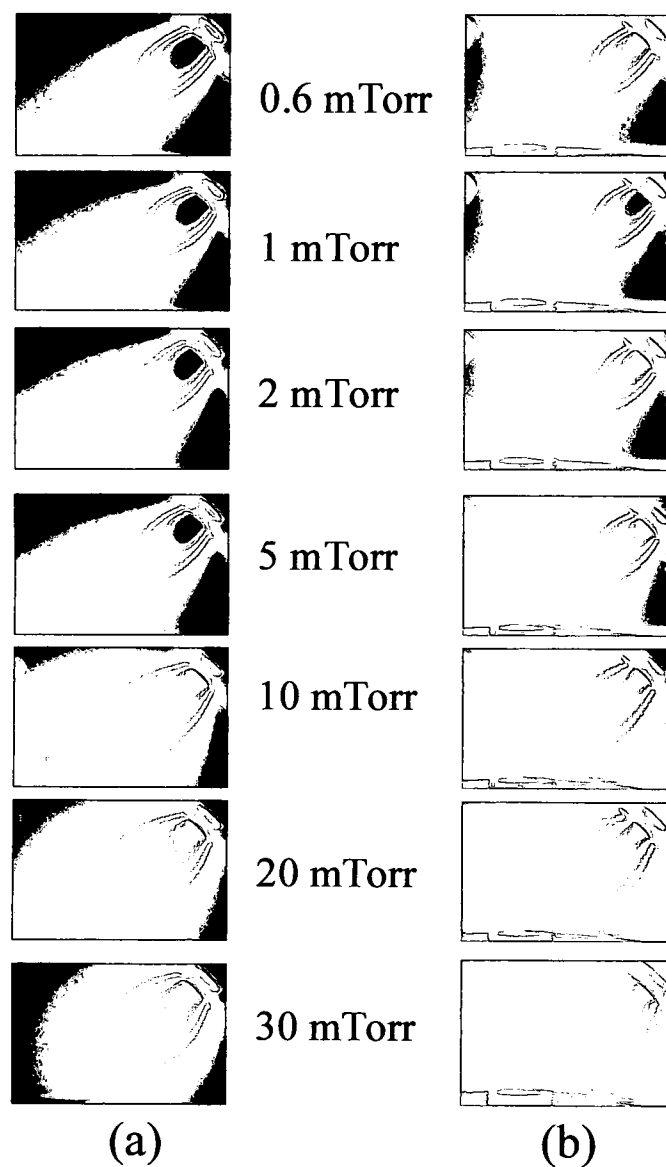
Table 3: All identified OES plasma species in IBPLD plasma processes

Molecule or Atom	Transition Terms	Laser Ablation (no ion-beam)	Ion-Beam (no laser ablation)	IBPLD
NO	$A^2\Sigma^+ \rightarrow X^2\Pi, v'=0, v''=3$	—	—	259.5
NO	$A^2\Sigma^+ \rightarrow X^2\Pi, v'=1, v''=5$	—	—	268.1
NO	$A^2\Sigma^+ \rightarrow X^2\Pi, v'=0, v''=5$	—	—	286.1
N <sub>2</sub>	$C^3\Pi_u \rightarrow B^3\Pi_g, v'=3, v''=1$	—	296.1	296.4
Al	$2D \rightarrow 2P^*$	307.7	—	307.8
Al	$2P^* \rightarrow 2D$	308.8	—	308.9
N <sub>2</sub>	$C^3\Pi_u \rightarrow B^3\Pi_g, v'=1, v''=0$	—	315.8	316.4
N <sub>2</sub> or N <sub>2</sub> <sup>+</sup>	$C^3\Pi_u \rightarrow B^3\Pi_g, v'=2, v''=2$	—	329.7	330.0
N <sub>2</sub>	$B^2\Sigma^+_u \rightarrow X^2\Sigma^+_g, v'=2, v''=0$	—	—	—
N <sub>2</sub>	$C^3\Pi_u \rightarrow B^3\Pi_g, v'=0, v''=0$	—	336.9	337.3
N <sub>2</sub> or N <sub>2</sub> <sup>+</sup>	$C^3\Pi_u \rightarrow B^3\Pi_g, v'=1, v''=2$	—	353.1	353.7
N <sub>2</sub>	$B^2\Sigma^+_u \rightarrow X^2\Sigma^+_g, v'=4, v''=3$	—	—	—
N <sub>2</sub> or N <sub>2</sub> <sup>+</sup>	$C^3\Pi_u \rightarrow B^3\Pi_g, v'=0, v''=1$	—	357.1	357.7
N <sub>2</sub> <sup>+</sup>	$B^2\Sigma^+_u \rightarrow X^2\Sigma^+_g, v'=1, v''=0$	—	—	—
Al	$2P^* \rightarrow 2S$	393.8	—	393.9
Al	$2P^* \rightarrow 2S$	395.6	—	395.7
NO	$B^2\Pi \rightarrow X^2\Pi$	—	—	410.9
NO	$B^2\Pi \rightarrow X^2\Pi, v'=1, v''=13$	—	—	411.9
N <sub>2</sub> <sup>+</sup>	$B^2\Sigma^+_u \rightarrow X^2\Sigma^+_g, v'=1, v''=2$	—	422.5	423.1
N <sub>2</sub>	$C^3\Pi_u \rightarrow B^3\Pi_g, v'=1, v''=5$	—	426.9	426.3
N <sub>2</sub> <sup>+</sup>	$B^2\Sigma^+_u \rightarrow X^2\Sigma^+_g, v'=0, v''=1$	—	—	428.4
O <sup>+</sup>	$2P^* \rightarrow 2S$	—	—	432.4
O <sup>+</sup>	$2S \rightarrow 2P^*$	—	—	447.1
O <sup>+</sup> or N <sub>2</sub>	$4P \rightarrow 4D^*$	—	466.8	467.2
N <sub>2</sub>	$C^3\Pi_u \rightarrow B^3\Pi_g, v'=0, v''=5$	—	—	—
N	$2P \rightarrow 2S^*$	—	491.8	492.4
N	$2P \rightarrow 2S^*$	—	493.9	494.5
O <sup>+</sup>	$2P^* \rightarrow 2P$	—	—	519.1
N <sup>+</sup>	$5P^* \rightarrow 5P$	—	532.9	533.5
N <sup>+</sup>	$5P \rightarrow 5D^*$	—	556.1	556.7
N	$4P^* \rightarrow 4P$	—	—	583.2
N <sup>+</sup>	$3D^* \rightarrow 3D$	—	648.5	649.2
O <sup>+</sup>	$2P \rightarrow 2S^*$	—	—	672.9
N	$4P \rightarrow 4S^*$	—	742.5	743.0
N	$4P \rightarrow 4S^*$	—	744.3	744.8
N	$4P \rightarrow 4S^*$	—	746.9	747.5
O	$5S^* \rightarrow 5P$	777.3	—	777.8
N	$4P \rightarrow 4P^*$	—	819.3	819.8
N	$4P \rightarrow 4P^*$	—	822.3	822.9
N	$4P \rightarrow 4P^*$	—	825.0	825.5
O	$3S^* \rightarrow 3P$	845.4	—	845.9
N	$2P \rightarrow 2P^*$	—	—	860.7
N	$2P \rightarrow 2P^*$	—	863.5	864.1
N	$4P \rightarrow 4D^*$	—	868.7	869.2

In addition to collecting optical emission spectra, the ICCD system was also used to explore the spatial distributions of plasma species in the IBPLD process. Figure 19 illustrates the effect changes in  $N_2$  pressure has on the plume interaction. Figure 19a shows the laser plume widening and eventually not even reaching the substrate in the 10  $\mu s$  snapshot as  $N_2$  pressure is increased. Figure 19b shows the synergistic effect of the plasma interaction as the pressure increases. As the background pressure is increased, the intense interaction between the two plasmas becomes apparent. Images of specific species in the plasmas were collected with a 10  $\mu s$  exposure gating using narrow band pass optical filters. Each filter allowed approximately 90% transmittance at the peak center. The background pressure was set to 20 mTorr for all filtered imaging to better view the plasma interaction. Figure 20 shows the original non-filtered image as well as the Al, N, and O filtered images. The Al image shows little interaction between the two plasmas, but the overall plume does appear to be shifted slightly towards the ion beam source. Both the N and O images show a large amount of interaction and additional excitation from the other plasma source. It was expected that the laser plume would create additional excitation from the laser plume due to the  $N_2$  background gas, but the ion beam source also produces additional O excitation from the  $Al_2O_3$  laser target.

### 3.2.2 Coatings Analysis

XPS analysis was performed in order to study the effect of pressure and ion energy on atomic composition. Figure 21 illustrates the dependence of atomic composition on chamber pressure while holding to a constant ion energy of 300 eV and a substrate bias of -200 V. Al content was largely unaffected by any pressure variation

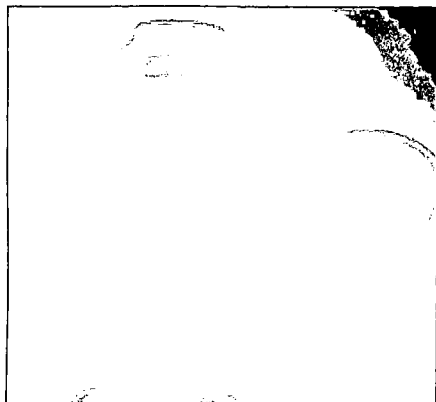


Emission intensity scale, a.u. (linear):

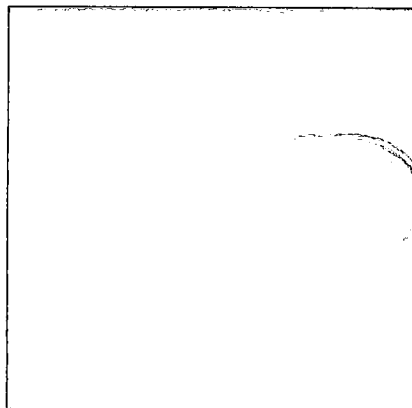
<1000	2000	4000	6000	8000	10000	>11000
-------	------	------	------	------	-------	--------

Figure 19: ICCD imaging of PLD of  $\text{Al}_2\text{O}_3$  target (a) and IBPLD process (b) with varying  $\text{N}_2$  background pressure

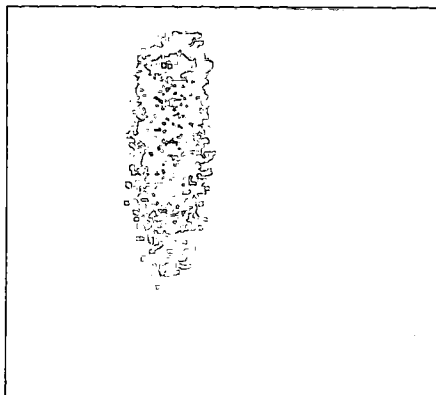
**a. No Filter**



**b. Al Filter – 391 nm**



**c. N Filter – 820nm**



**d. O Filter – 780 nm**

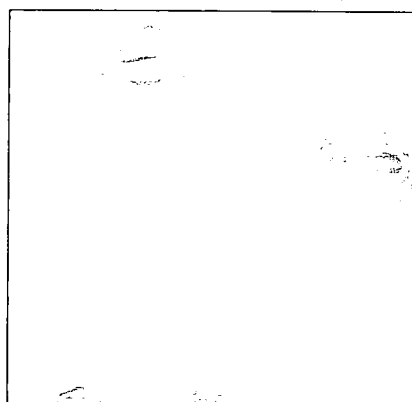


**Figure 20: IBPLD of Al<sub>2</sub>O<sub>3</sub> target in N<sub>2</sub> background at 20 mTorr with spectral filters**

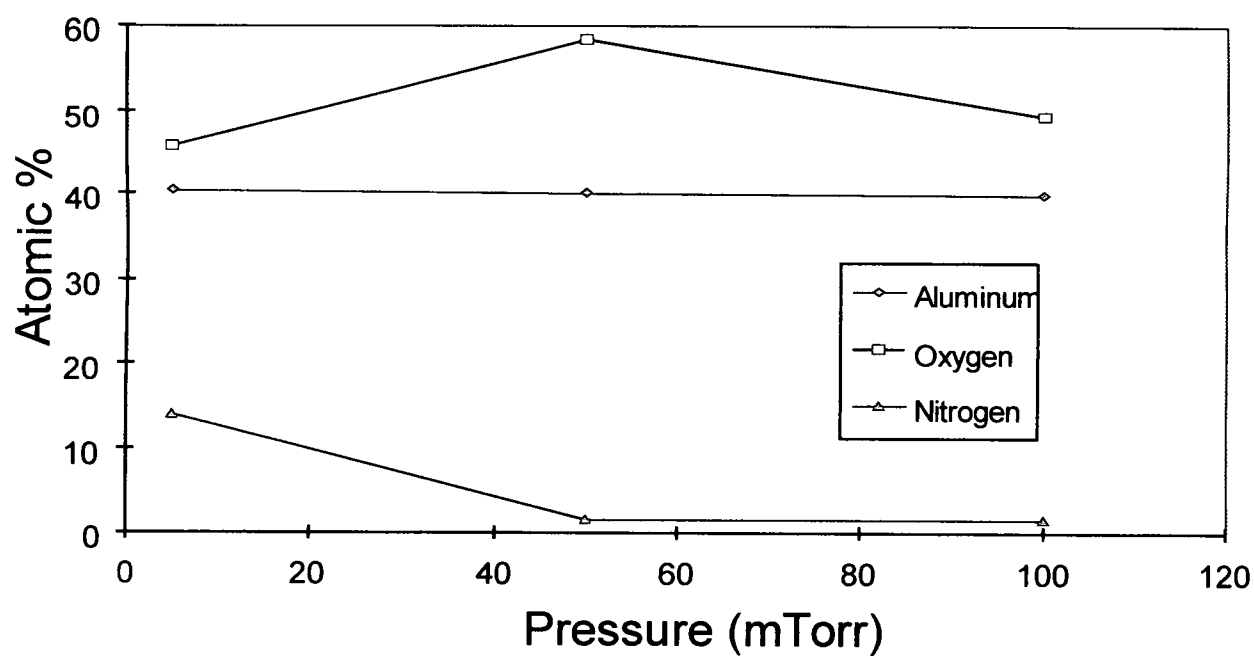


Figure 21: Background N<sub>2</sub> gas pressure versus atomic composition of sample as determined by XPS

while N content dropped with increasing pressure. The content of O first increases with an increase temperature, but after about 50 mTorr, it begins to decrease while the pressure increases. There is some uncertainty in atomic compositional analysis with XPS as shown in the low pressure analysis depicted in Figure 22. At 1 Torr, the two samples are separated by 0.08, which would indicate an error as much as  $\pm 0.04$ , which would translate to a 3-4% error in the measurement of atomic composition.

Since pitting and holes in the coating were observed at pressures above 50 mTorr and the higher pressure creates coatings with atomic compositions further from stoichiometric ratios, a low pressure was chosen for the next atomic composition analysis. The low pressure versus composition analysis was comprised of coatings deposited from 0.6 to 15 mTorr. Figure 22 continues the trend that lower pressures increase N content in the coating. At 0.6mTorr, the coating's atomic content was nearly a 1:2 ratio between N and Al. Figure 23 depicts the analysis of ion energy versus atomic composition where the pressure was set at 5 mTorr and a substrate bias of -200V was applied. Overall, as ion energy was increased, both Al and N showed a steady increase in atomic content, while the O slowly decreased in content.

XRD analysis was performed in order to examine the crystallinity on the coating. The substrate temperature was set at 330°C in 1 mTorr of N<sub>2</sub> and an ion beam energy of 300 eV for the XRD analysis samples. In one sample no bias was applied and in the other, a -200 V bias was applied to the substrate. Coatings grown on a grounded substrate showed only Fe peaks (Figure 24) indicating an amorphous structure [44]. The -200 V bias on the substrate yielded a crystalline structure. The peaks match the diffraction pattern for the hexagonal Al<sub>10</sub>N<sub>8</sub>O<sub>3</sub> phase. Due to the fact that the peaks are

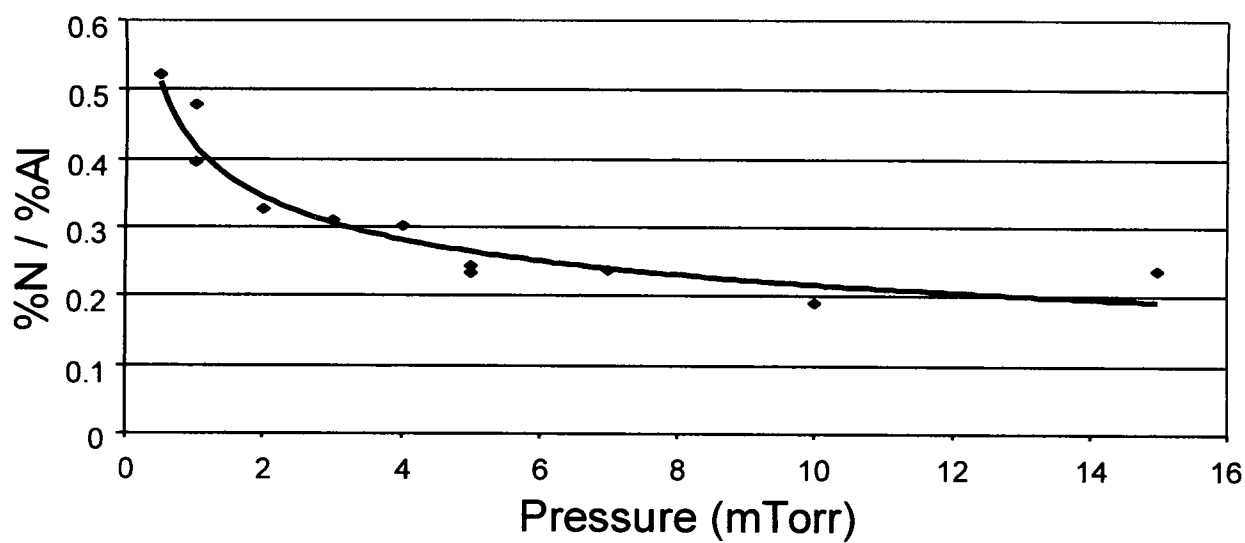


Figure 22: Background N<sub>2</sub> gas pressure versus N%/Al% ratio in sample as determined by XPS

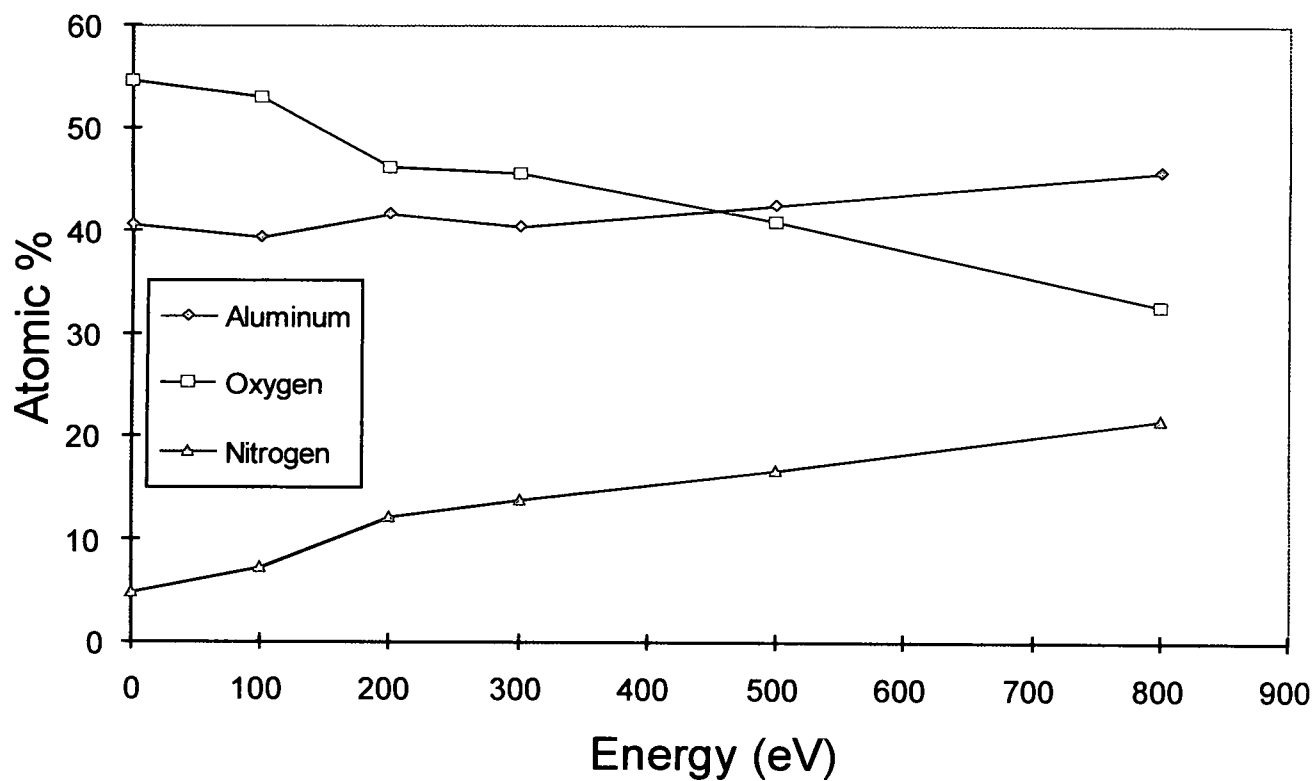


Figure 23: Ion beam energy versus atomic composition of sample as determined by XPS



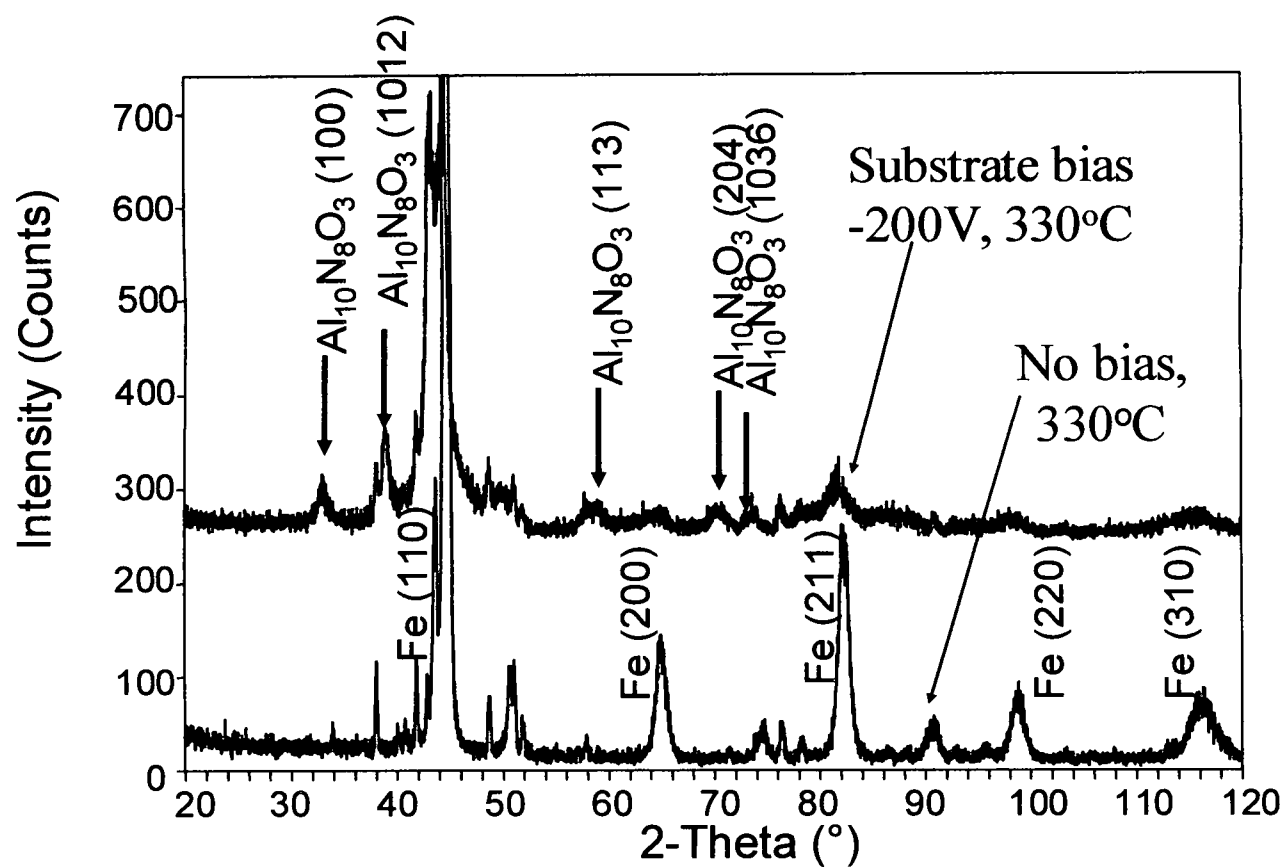


Figure 24: XRD of Al-O-N samples with and without substrate bias

small and relatively wide, it can be deduced that the film contains small crystalline phases in an amorphous Al-O-N matrix. The Al-O-N matrix also was oxygen rich as indicated by the XPS data indicating a higher O content than N content.

### 3.2.3 Discussion

The coatings grown with the IBPLD process had an amorphous Al-O-N matrix with embedded hexagonal  $\text{Al}_{10}\text{N}_8\text{O}_3$  nanocrystals. Conditions for the growth of the most stoichiometric coating were a pressure of 0.6 mTorr, a temperature of 330°C, 800 eV on the ion beam source, and a substrate bias of -200V.

With the results of the OES analysis from Table 3, the chemical composition data from the XPS, and the crystallographic data from the XRD, a mechanism for the creation of the Al-O-N can be proposed. It appears that the NO species along with the higher energy O and N species are a large factor in the growth of the Al-O-N. Emission bands for either AlO or AlN molecules were not detected in the combined plasma. The absence of these species suggest that the growth mechanism requires the higher energy ions from the oxygen and nitrogen, but the aluminum ions, which had no real change from the PLD to the IBPLD, play less of a role. Having no AlO and AlN in the plasma suggests that the higher energy does not play a role in the plasma away from the substrate, but on the substrate surface itself. Having this greater energy the ions move about more freely and form the Al-O-N coating. This more extensive interaction between the O and N can be seen in Figure 20. In both the O and N image, a plasma channel can be observed between the two plasma sources. The laser ablation process further exciting the  $\text{N}_2$  gas would not be unexpected because the gas pressure is equal throughout the chamber. The big

surprise is that the O released from the PLD process that does not reach the target is further excited by the ion beam source. Unfortunately, a NO image was unable to be collected due to the NO filter being in the ultraviolet (UV) range (280 nm). The 35 mm focusing optics for the ICCD system is not made of UV transparent glass, so capturing an image in the UV range is not possible. Having the ability to obtain a more direct analysis of the NO species in the plasma would be ideal with UV transparent focusing optics, but the image would likely be very similar to the O and N interaction in Figure 20. This assumption can be made because of the plasma channel between the two sources and the secondary excitation of the O from the ion beam and the N from the laser ablation plume. The IBPLD mechanism for the formation of the NO species in very low pressure plasmas at low energies correlates to other published sources on N and O plasma interactions [45-47].

With the ICCD imaging system not only can plasma chemistry be studied, but plume shape can be examined as well. Varying the pressure from 0.6 mTorr to 30 mTorr in Figure 19 causes the plume shape to change from a narrower and elongated plume, to a fatter plume that no longer reaches the substrate in the 10  $\mu$ s snapshot. Plume background shape is governed by a cosine-power law that depends upon the collision scattering effects from a background gas [48]. At low pressure the plume shape matches the  $\cos^n(\Theta)$  angular distribution where  $n > 7$ . By the time the pressure had reached higher pressures, the spherical plume shape corresponded to a value where  $n = 2-3$ .

An area that warrants further study is imaging of the NO species for spatial and temporal analysis. It has been demonstrated to be an important factor in the deposition mechanism for Al-O-N and may hold the key to further improve the stoichiometric

distribution in the coating. Another area to study would be the OES at different pressures to correlate to the ICCD imaging at different pressures. Different pressures may yield different spectral peaks and/or distributions.

### **3.3 Analysis and Discussion of MSPLD of Yttria Stabilized Zirconia and Molybdenum Nanocomposite**

#### **3.3.1 Plasma Diagnostics Analysis**

To analyze the timing of the magnetron plasma, a DPO with voltage and current probes was used. Voltage and current waveforms were collected for a magnetron operating at a 120 kHz, which equates to it firing every 8.3  $\mu\text{s}$  (Figure 25). Each magnetron pulse is broken down into three distinct modes: 1) initiation and sputtering, 2) shutoff and recovery, and 3) voltage transition for reinitiation. The initiation and sputtering mode lasts for 3.3  $\mu\text{s}$  (5-8.3  $\mu\text{s}$  in Figure 25) and is initiated by a large current spike. The large negative voltage maintains the sputtering process until the shutoff and recovery mode. The shutoff and recovery mode lasts for 3  $\mu\text{s}$  and features a large swing in voltage polarity to arrest the sputtering process and uncharge the sample which would charge up because the YZS target is an insulator (8.3-11.3  $\mu\text{s}$  in Figure 25). The remaining 2  $\mu\text{s}$  ranging from 11.3 to 13.3  $\mu\text{s}$  features a voltage transition to prepare for the next magnetron sputtering pulse. Because the DPO could only trigger the laser to fire from a rising or falling edge on the wave form, the rising edge at beginning of the shutoff and recovery mode was chosen as time zero for all synchronization events.

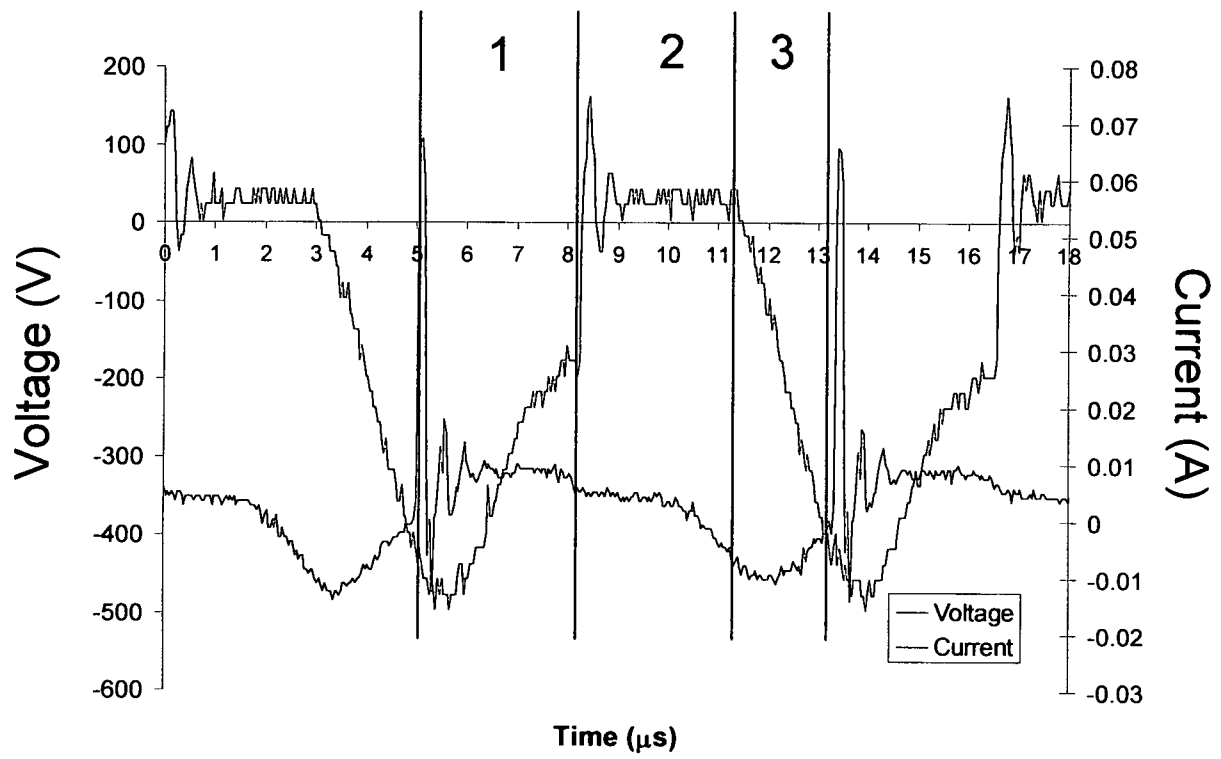


Figure 25: Voltage and current waveforms versus time for the magnetron in the MSPLD process with 1) initiation and sputtering, 2) shutoff and recovery, and 3) voltage transition for reinitiation operational modes

TOF analysis was used in order to explore the timing of the laser plume and determine the synchronization times between the magnetron and laser.  $\text{Zr}^*$  (470 nm) and  $\text{ZrO}^*$  (480 nm) narrow bandpass filters were used on the PMT to analyze the two most abundant species in the plasma pulse (Figure 26). The analysis was carried out at 800 mJ laser energy in a 10 mTorr Ar atmosphere. The collimating tube was placed approximately half way between the target and the substrate (approximately 4 cm). After the initial laser pulse (0-1  $\mu\text{s}$ ) there is a large drop in intensity as fewer emitting particles pass by the PMT. From 2-3  $\mu\text{s}$ , there is an intensity increase as the main bulk of the plume approaches the detector. The maximum intensity for both species occurs at approximately 3 to 3.25  $\mu\text{s}$ , after which they dissipate back to the background by 9  $\mu\text{s}$ . From Figure 26, one can deduce that a single laser ablation plume persists for around 9  $\mu\text{s}$  before striking the substrate.

Gated ICCD imaging was used to study the temporal and spatial plume distribution and interaction. Figure 27 shows the typical magnetron plasma and PLD plume interaction. Figure 28, at first, also shows a typical magnetron and PLD plume interaction, but it also shows a secondary interaction and emission. In both figures, the laser fires at 1  $\mu\text{s}$ . In the first 5  $\mu\text{s}$  the plume is visible as it moves toward the substrate. Over the next 5  $\mu\text{s}$ , the plume dissipates as it would in a stand alone PLD process. In the typical magnetron and laser firing cycle in Figure 27, the plume continued to dissipate from the 10  $\mu\text{s}$  to 15  $\mu\text{s}$  as expected, but at 12  $\mu\text{s}$  image (outlined in red) in Figure 28, there is secondary emission from both the magnetron and the laser plume. This secondary excitation effect only occurred in the MSPLD process for the 1  $\mu\text{s}$  (0.7  $\mu\text{s}$ ) and 6  $\mu\text{s}$

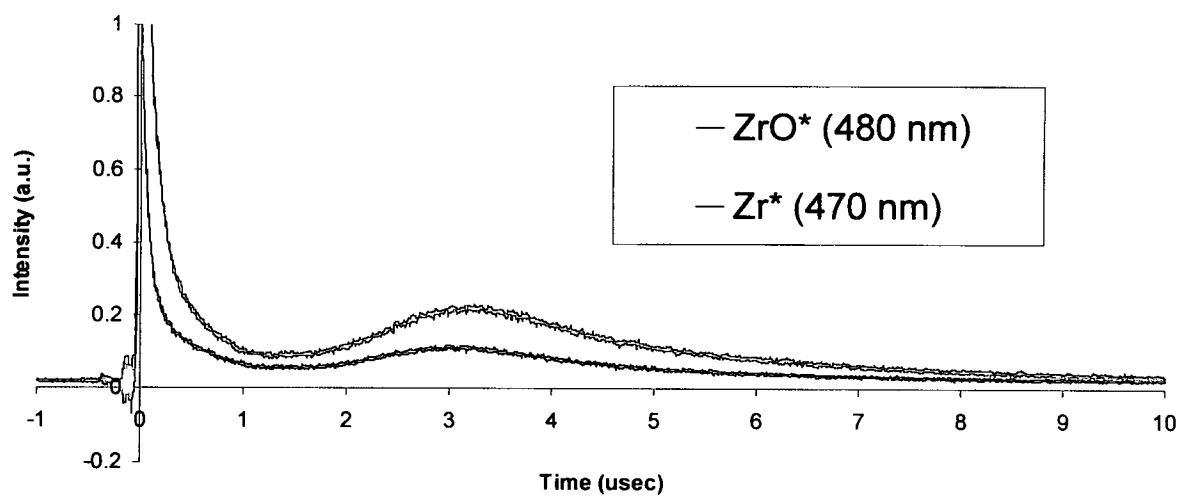


Figure 26: TOF waveforms of PLD of YSZ target

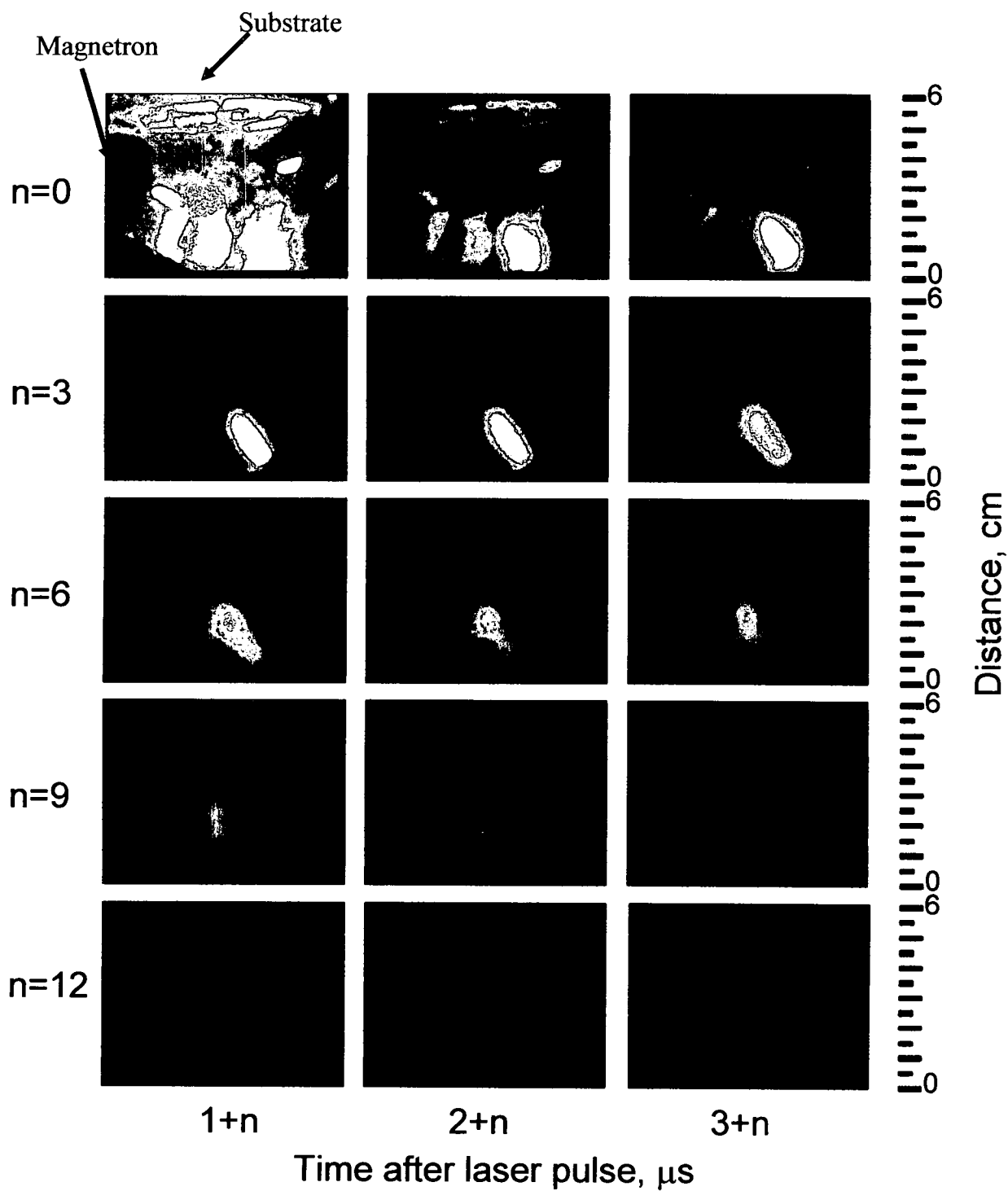


Figure 27: ICCD imaging of MSPLD process with a typical laser plume response



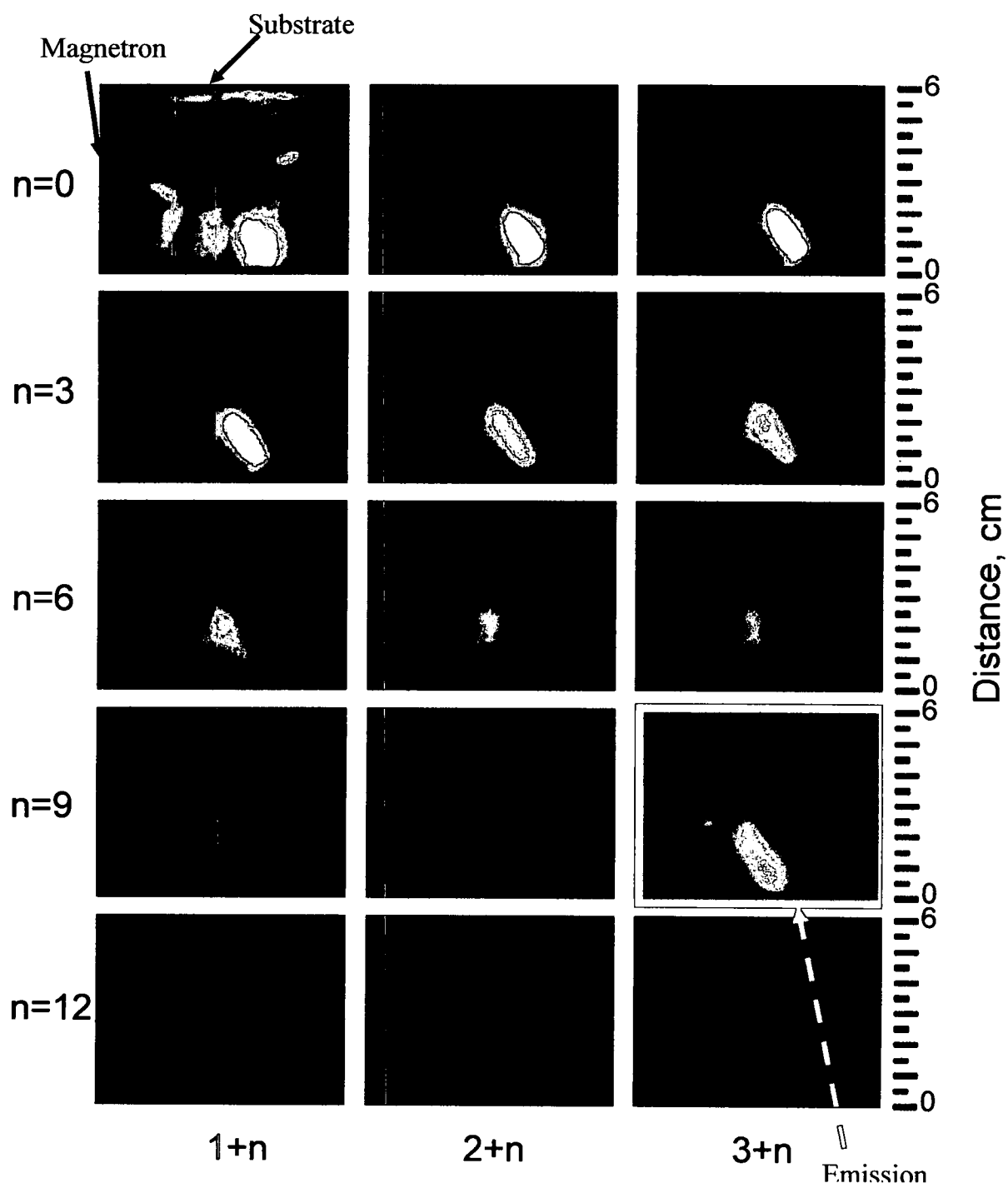


Figure 28: ICCD imaging of MSPLD process with a secondary laser plume interaction and emission response

synchronization delay times. As an example, Figure 29 illustrates the timing sequence between the magnetron and the laser at a synchronization delay of 6  $\mu\text{s}$ . The rising edge of the voltage waveform is at time zero, and the ZrO\* TOF shows the laser peak at 6  $\mu\text{s}$ . Other delay times and non-synchronized operation showed no additional excitation.

### 3.3.2 Coatings Analysis

The YSZ/Mo non-synchronized, 0.7  $\mu\text{s}$  synchronization delay, 4  $\mu\text{s}$  synchronization delay, and 6  $\mu\text{s}$  synchronization delay coatings were analyzed with XPS and XRD. XPS scans (Table 4) showed little change in atomic composition between the non-synchronized and synchronized samples. The greatest change was in the Mo content which ranged from 2.0 to 13.2 at. %. Yttrium ranged between 1.7 and 1.9 at. %, Zr ranged from 23.5 to 29.9 at. %, and O ranged from 60.6 to 61.6 at. %. XRD was used to identify crystallographic planes present in each sample. In Figure 30, the blue line is the sample that was deposited with no synchronization between the magnetron and the laser. The only peak is the Fe from the stainless steel substrate. The rest of the scan features indicate an amorphous structured coating. The 1  $\mu\text{s}$  and 6  $\mu\text{s}$  synchronization delay sample XRD scans are the green line and the orange line, respectively. These scans both had defined peaks at 27.7° and 29.6° two-theta, as well as smaller higher order peaks ranging from 32.8° to 70° two-theta. These two main peaks correspond to 27.5° and 30.3° two-theta peaks from the orthorhombic ZrO<sub>2</sub> structure [49]. The red line in Figure 30 is the 4  $\mu\text{s}$  synchronization sample. As in the non-synchronized sample, only the Fe peak from the substrate is visible along with amorphous crystallographic features.

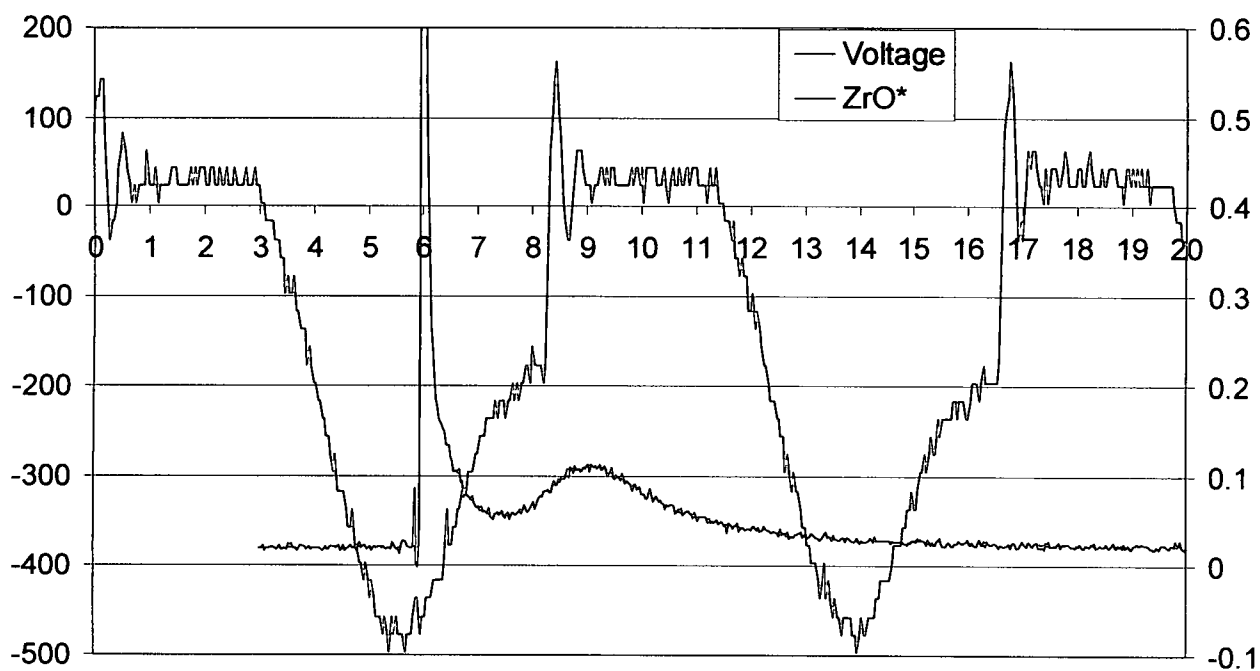


Figure 29: Voltage waveform and ZrO<sup>\*</sup> TOF at 6 μs synchronization delay for laser trigger from magnetron

Table 4: Atomic composition of MSPLD coatings with no synchronization, 1  $\mu\text{s}$  delay synchronization, and 6  $\mu\text{s}$  delay synchronization as determined by XPS

<b>Element</b>	<b>No Sync</b>	<b>1 <math>\mu\text{s}</math> Delay</b>	<b>6 <math>\mu\text{s}</math> Delay</b>
Y	1.7	1.9	1.9
Zr	23.5	29.9	26.6
Mo	13.2	2.0	11.0
O	61.6	66.2	60.6

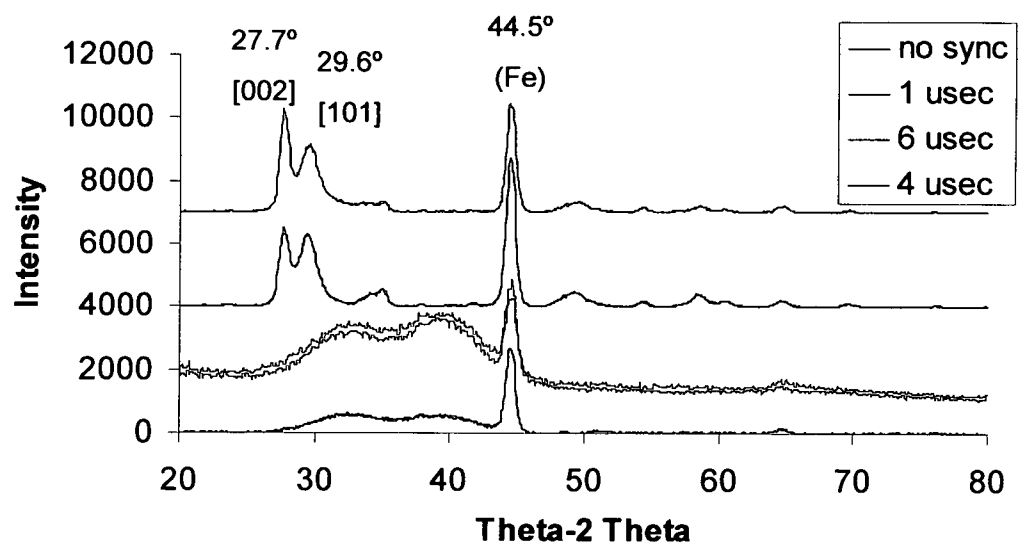


Figure 30: XRD scans of YSZ/Mo nanocomposite coatings with no synchronization, 1 $\mu$ s synchronization, 4  $\mu$ s synchronization, and 6  $\mu$ s synchronization

### 3.3.3 Discussion

The key link between the plasma data and the coating data is the crystallinity observed from the XRD data and the secondary excitation effect observed with the ICCD imaging, both of which occurred only at 1  $\mu\text{s}$  and 6  $\mu\text{s}$  synchronization delay times. In the 1  $\mu\text{s}$  and 6  $\mu\text{s}$  delay samples, orthorhombic  $\text{ZrO}_2$  nanocrystals were observed in the amorphous Mo matrix. The effect that created the nanocrystalline phases was the operation of the arc suppressor on the DC pulsed power supply. The arc suppression circuitry in the DC pulsed power supply monitors the current in the plasma. As illustrated in Figure 25, there is a large current peak at the moment the glow discharge is initiated. If extra electrons were to be injected into the plasma at a different time, this would cause a current spike and the power supply would respond as it would to an arc event at the target. These extra electrons could originate from another high energy plasma in close proximity to the glow discharge from the magnetron, such as a laser ablation plasma plume. Upon detection of the assumed arc, the power supply would shut down. The arc suppression circuitry takes between 5  $\mu\text{s}$  and 200  $\mu\text{s}$  to recover and restart the sputtering process. The delay times between the firing of the laser and the magnetron would strike at different points in the 8.3  $\mu\text{s}$  cycle time of the magnetron. This could affect the how long it takes the circuitry to recover or even if it detects the increased current as an arc event. The 1  $\mu\text{s}$  delay sample contained only 2.0 at. % Mo indicating the suppression circuitry may have been shutoff for an extended period of time versus the 6  $\mu\text{s}$  delay sample which contained 10.0 at. % Mo. Both samples were below the 13.2 at. % Mo content in the non-synchronized sample indicating they both were not running uninterrupted.

This arc suppression effect can be seen in the ICCD imaging as well. After the power supply shuts down to arrest a detected arc event, it would take a greater voltage spike than usual to initiate a new plasma as opposed to continuing the sputtering process with a dissipating plasma from the previous cycle. This extra large spike can be seen in the 12  $\mu$ s image from the interaction and emission response. The extra energy excites and ionizes the slower neutrals at the end of the laser ablation plume causing nanocrystalline phases to form. These nanocrystalites eventually land on the substrate and become incorporated into the film. These are the orthorhombic  $\text{ZrO}_2$  nanocrystals observed in the XRD scans. The minimum pressure and temperature needed to form orthorhombic  $\text{ZrO}_2$  is 1.8 gigapascals (GPa) and 840 K (587°C) [50]. With this process,  $\text{ZrO}_2$  can be crystallized in 30 mTorr by MSPLD at a temperature of 200°C.

## CHAPTER 4

### CONCLUSIONS

Plasma chemistries and the functionalization of multi-walled carbon nanotubes were studied by optical emission spectroscopy, X-ray photoelectron spectroscopy, and scanning electron microscopy. Plasma treatments were carried out in backgrounds of Ar, N<sub>2</sub>, and H<sub>2</sub> gas mixtures. It was demonstrated that Ar/N<sub>2</sub> plasma mixtures created more surface etching and functionalization than Ar/H<sub>2</sub> gas mixtures. It was also demonstrated that an increase in N<sub>2</sub> content in an Ar/N<sub>2</sub> plasma led to an increase in N<sup>+</sup> species. This N<sup>+</sup> species increase is hypothesized to be responsible for the increase in CNT functionalization. The concentration of H<sub>2</sub> in an Ar/H<sub>2</sub> plasma experienced a linear decrease in intensity with a drop in H<sub>2</sub> concentration. The current plasma functionalization of CNTs study was also compared to recent studies in plasma functionalization with remote plasma sources versus the sample stage cathode method used for this study.

Ion beam assisted pulsed laser deposition was used to deposit an Al-O-N coating from a N<sub>2</sub> precursor gas and an Al<sub>2</sub>O<sub>3</sub> laser target. The plasma interaction and resulting coating were analyzed by high speed synchronized plasma imaging, optical emission spectroscopy, X-ray photoelectron spectroscopy, and X-ray diffraction. The result of these analyses showed that at low pressures, higher energy N, O, and NO species created



in the plasma channel are instrumental in the creation of Al-O-N. It was further shown that the higher energy species participate in the surface reactions at the substrate. This surface reaction not only created near stoichiometric ratios of Al, O, and N, but created nanocrystalline  $\text{Al}_{10}\text{N}_8\text{O}_3$  phases in the amorphous matrix. By correlating the plasma data to the resulting coatings, new methods of controlling IBPLD processes have been demonstrated.

Magnetron sputtering combined with pulsed laser deposition was used to deposit nanocrystalline  $\text{ZrO}_2$  in a Mo matrix from a YSZ laser target and Ar sputtering of a Mo magnetron target. The plasma interactions as well as the deposited coating were analyzed by TOF analysis, high speed synchronized plasma imaging, X-ray photoelectron spectroscopy, and X-ray diffraction. The resulting coatings that were at 1  $\mu\text{s}$  and 6  $\mu\text{s}$  synchronization delay were the only coatings that showed nanocrystalline YSZ. All other synchronization times and non-synchronized operation between the laser and magnetron produced amorphous YSZ in the Mo matrix. The ICCD imaging system captured an image at 12  $\mu\text{s}$  in the 1  $\mu\text{s}$  synchronization delay showing the secondary excitation that produced the nanocrystalline orthorhombic  $\text{ZrO}_2$  phase. This excitation was due to the arc suppression circuitry detecting incoming electrons from the laser ablation plume causing the power supply to shut down mid cycle. After a delay, the supply would reignite a new plasma and excite the slower neutral species still en route to the substrate. This arc suppression effect can be seen in the final film stoichiometries with lower concentrations of Mo in the final coating for the 1  $\mu\text{s}$  and 6  $\mu\text{s}$  synchronization delay times.

In each of these three nanostructured material examples, a plasma property was correlated to a coating/material property through in situ and ex situ diagnostic methods. With these correlations and real-time feedback from the in situ plasma diagnostics, real-time process control can be integrated into each deposition or plasma treatment. With this new control scheme, nanostructured materials can be manufactured with greater control which will lead to highly reproducible product with improved quality. As this area of nanostructured material research continues to mature, more of these nanostructured materials will find their way into products that will affect our everyday lives.

## REFERENCES

- 1 Voevodin, A.A. and Zabinski, J.S., 2004, Smart Nanocomposite Coatings with Chameleon Surface Adaptation in Tribological Applications, in *Nanostructured Thin Films and Nanodispersion Strengthened Coatings*, Kluwer Academic, Dordrecht: 1-8.
- 2 Brandt, C., Testrich, H., Kozakov, R., and Wilke, C., 2006, Investigation of the disturbance of a Langmuir probe and its influence on measurement results, *Review of Scientific Instruments* 77: 023504-023505.
- 3 Brundle, C.R., 1992, X-Ray Photoelectron Spectroscopy, in *Encyclopedia of Materials Characterization - Surfaces, Interfaces, and Thin Films*, Butterworth-Heinemann, Boston: 282-299.
- 4 Toney, M.F., 1992, X-Ray Diffraction, in *Encyclopedia of Materials Characterization - Surfaces, Interfaces, and Thin Films*, Butterworth-Heinemann, Boston: 198-213.
- 5 White, W.B., 1992, Raman Spectroscopy, in *Encyclopedia of Materials Characterization - Surfaces, Interfaces, and Thin Films*, Butterworth-Heinemann, Boston: 428-441.
- 6 Bindell, J.B., 1992, Scanning Electron Microscopy, in *Encyclopedia of Materials Characterization - Surfaces, Interfaces, and Thin Films*, Butterworth-Heinemann, Boston: 70-84.
- 7 Sickafus, K.E., 1992, Transmission Electron Microscopy, in *Encyclopedia of Materials Characterization - Surfaces, Interfaces, and Thin Films*, Butterworth-Heinemann, Boston: 99-116.
- 8 Demidov, V. I., Ratynskaia, S. V., and Rypdal, K., 2002, Electric probes for plasmas: The link between theory and instrument, *Review of Scientific Instruments* 73: 3409-3439.
- 9 Chapman, B., 1980, Plasmas, in *Glow Discharge Processes*, John Wiley & Sons, Inc., New York: 60-64.
- 10 Chen, F.F., 1965, Electric Probes, in *Plasma Diagnostic Techniques*, Academic Press, New York: 113.
- 11 Allen, J. E., Boyd, R. L. F., and Reynolds, P., 1957, The Collection of Positive Ions by a Probe Immersed in a Plasma, *Proceedings of the Physical Society B* 70: 297-304.
- 12 C. Muratore, thesis, Colorado School of Mines (2002).

- 13 Tissue, B.M., 2000, Quadrupole Mass Spectrometry. <http://www.chem.vt.edu/chem-ed/ms/quadrupo.html>.  
Ref Type: Electronic Citation
- 14 Geohegan, D.B., 1994, Diagnostics and Characteristics of Laser-Produced Plasmas, in *Pulsed Laser Deposition of Thin Films*, John Wiley & Sons, Inc., New York: 115-165.
- 15 Ocean Optics, 2007, Spectrometer Operating Principles.  
<http://www.oceanoptics.com/technical/operatingprinciples.asp>.  
Ref Type: Electronic Citation
- 16 Jones, J. G., Voevodin, A. A., and Zabinski, J. S., 2001, Characterization of plume fluence for laser ablation of yttria stabilized zirconia in mixed oxygen and argon environments, *Surface and Coatings Technology* 146-147: 258-262.
- 17 Iijima, S., 1991, Helical Microtubules of Graphitic Carbon, *Nature* 354: 56-58.
- 18 Dickrell, P. L., Pal, S. K., Bourne, G. R., Muratore, C., Voevodin, A. A., Ajayan, P. M., Schadler, L. S., and Sawyer, W. G., 2006, Tunable friction behavior of oriented carbon nanotube films, *Tribology Letters* V24: 85-90.
- 19 Reade, R. P., Berdahl, P., Russo, R. E., and Garrison, S. M., 1992, Laser deposition of biaxially textured yttria-stabilized zirconia buffer layers on polycrystalline metallic alloys for high critical current Y-Ba-Cu-O thin films, *Appl.Phys.Lett.* 61: 2231-2233.
- 20 Six, S., Gerlach, J. W., and Rauschenbach, B., 2001, Ion beam assisted pulsed laser deposition of epitaxial aluminum nitride thin films on sapphire substrates, *Surface and Coatings Technology* 142-144: 397-401.
- 21 Huhne, R., Beyer, C., Holzapfel, B., Oertel, C. G., Schultz, L., and Skrotzki, W., 2001, Formation and destruction of cube texture in MgO films using ion beam assisted pulsed laser deposition, *Journal of Applied Physics* 90: 1035-1039.
- 22 Bysakh, S., Chattopadhyay, K., Ling, H., Wu, J. D., Dong, C., Wang, Y. Q., Duan, X. F., and Kuo, K. H., 2004, A study of nanostructures of thin films in B-C-N system produced by pulsed laser deposition and nitrogen ion-beam-assisted pulsed laser deposition, *Journal of Materials Research* 19: 759-767.
- 23 Ren, Z. M., Lu, Y. F., Ho, D. H. K., Chong, T. C., Cheong, B. A., Pang, S. I., Wang, J. P., and Li, K., 1999, Raman Spectroscopy Studies of the Influence of Substrate Temperature and Ion Beam Energy on CN<sub>x</sub> Thin Films Deposited by Nitrogen-Ion-Assisted Pulsed Laser Deposition, *Jpn.J.Appl.Phys.* 38: 4859-4862.
- 24 A.A.Voevodin, M.A.Capano, A.J.Safriet, M.S.Donley, and J.S.Zabinski, 1996, Combined magnetron sputtering and pulsed laser deposition of carbides and diamond-like carbon films, *Appl.Phys.Lett.* 69: 188-190.

- 25 Voevodin, A. A., Fitz, T. A., Hu, J. J., and Zabinski, J. S., 2002, Nanocomposite tribological coatings with "chameleon" surface adaptation, *Journal of Vacuum Science & Technology A: Vacuum, Surfaces, and Films* 20: 1434-1444.
- 26 Jones, J. G., Muratore, C., Waite, A. R., and Voevodin, A. A., 2007, Plasma Treatment of Carbon Nanotubes, *Journal of Vacuum Science & Technology B*.
- 27 Voevodin, A. A., Jones, J. G., Zabinski, J. S., and Waite, A. R., 2007, Plasma Interaction Effects in Ion-Beam Assisted Pulsed Laser Deposition of Al-O-N Films, *Journal of Applied Physics*.
- 28 Zabinski, J. S., Hu, J. J., Bultman, J. E., Pierce, N. A., and Voevodin, A. A., 2007, Stoichiometry and characterization of aluminum oxynitride thin films by ion-beam-assisted pulsed laser deposition, *Thin Solid Films*.
- 29 Jones, J. G., Muratore, C., Waite, A. R., and Voevodin, A. A., 2006, Plasma diagnostics of hybrid magnetron sputtering and pulsed laser deposition, *Surface and Coatings Technology* 201: 4040-4045.
- 30 2006, NIST Atomic Spectra Database.  
<http://physics.nist.gov/PhysRefData/ASD/index.html>, Version 3.1.0.  
 Ref Type: Electronic Citation
- 31 Chen, L. Y., Cheng, C. Y., and Chau-Nan Hong, F., 2002, Properties of carbon nitride (CN<sub>x</sub>) films deposited by a high-density plasma ion plating method, *Diamond and Related Materials* 11: 1172-1177.
- 32 Khandelwal, A., Niimi, H., Lucovsky, G., and Lamb, H. H., 2002, Low-temperature Ar/N<sub>2</sub> remote plasma nitridation of SiO<sub>2</sub> thin films, *Journal of Vacuum Science & Technology A: Vacuum, Surfaces, and Films* 20: 1989-1996.
- 33 Liu, X. W., Lin, J. H., Tseng, C. H., and Shih, H. C., 2001, Optical and structural properties of the amorphous carbon nitride by ECR-plasma, *Materials Chemistry and Physics* 72: 258-263.
- 34 Liu, Y., Liu, L., Liu, P., Sheng, L., and Fan, S., 2004, Plasma etching carbon nanotube arrays and the field emission properties, *Diamond and Related Materials* 13: 1609-1613.
- 35 Seo, H., Kim, J. H., Chung, K. H., Kim, J. Y., Kim, S. H., and Jeon, H., 2005, Characterization of remote inductively coupled CH<sub>4</sub>-N<sub>2</sub> plasma for carbon nitride thin-film deposition, *Journal of Applied Physics* 98: 043308.
- 36 Voevodin, A. A., Jones, J. G., Zabinski, J. S., and Hultman, L., 2002, Plasma characterization during laser ablation of graphite in nitrogen for the growth of fullerene-like CN<sub>x</sub> films, *Journal of Applied Physics* 92: 724-735.

- 37 Moulder, J.F., Stickle, W.F., Sobol, P.E., and Bomben, K.D., 1995, *Handbook of X-Ray Photoelectron Spectroscopy*, Physical Electronics, Inc., Eden Prairie.
- 38 Lide, D.R., 1995, Atomic, Molecular, and Optical Physics, in *CRC Handbook of Chemistry and Physics*, 274-279.
- 39 Muratore, C., Walton, S. G., Leonhardt, D., Fernsler, R. F., Blackwell, D. D., and Meger, R. A., 2004, Effect of plasma flux composition on the nitriding rate of stainless steel, *Journal of Vacuum Science & Technology A: Vacuum, Surfaces, and Films* 22: 1530-1535.
- 40 Muratore, C., 2007.  
Ref Type: Unpublished Work
- 41 Khare, B., Wilhite, P., Tran, B., Teixeira, E., Fresquez, K., Mvondo, D. N., Bauschlicher, C., and Meyyappan, M., 2005, Functionalization of Carbon Nanotubes via Nitrogen Glow Discharge, *J.Phys.Chem.B* 109: 23466-23472.
- 42 Pearse, R.W.B. and Gaydon, A.G., 1976, *The Identification of Molecular Spectra*, John Wiley & Sons, Inc., N.Y.: 407.
- 43 1995, *NIST Database for Atomic Spectroscopy*, NIST.
- 44 JCPDS Powder Diffraction File, 1998, PDF Card #06-0696. Swarthmore, PA, International Center for Powder Diffraction Data.  
Ref Type: Data File
- 45 Broc, A., Benedictis, S. D., and Dilecce, G., 2004, LIF investigations on NO, O and N in a supersonic N<sub>2</sub>/O<sub>2</sub>/NO RF plasma jet, *Plasma Sources Science and Technology* 13: 504-514.
- 46 Ricard, A. and Monna, V., 2002, Reactive molecular plasmas, *Plasma Sources Science and Technology* 11: A150-A153.
- 47 Ricard, A., Monna, V., Blanchard, H., Trichard, J.L., and Hivert, D., 2001, Density of N and O Atoms in a Flowing Post-Discharge Reactor of Industrial Scale (900 Litres), 195-197.
- 48 Saenger, K.L., 1994, Angular Distribution of Ablated Material, in *Pulsed Laser Deposition of Thin Films*, John Wiley & Sons, Inc., New York: 199-227.
- 49 JCPDS Powder Diffraction File, 1998, PDF Card #41-0017. Swarthmore, PA, International Center for Powder Diffraction Data.  
Ref Type: Data File
- 50 Fadda, G., Truskinovsky, L., and Zanzotto, G., 2002, Unified Landau description of the tetragonal, orthorhombic, and monoclinic phases of zirconia, *Phys.Rev.B* 66: 174107.

R002593069